UNIVERSIDAD DE CONCEPCIÓN
FACULTAD DE CIENCIAS FÍSICAS Y MATEMÁTICAS

Morpho-kinematical analysis of ionized gas in two cluster AGN at half the age of the universe

Análisis morfo-cinemático del gas ionizado en dos AGN de cúmulo a la mitad de la edad del universo

By: Marcela Yasmín González Paillalef

Tesis presentada a la Facultad de Ciencias Físicas y Matemáticas de la Universidad de Concepción para optar al grado académico de Magíster en Astronomía

Marzo 2021

Concepción, Chile

Profesor Guía: Ricardo Javier Demarco López

Colaborador: Héctor Flores

AGRADECIMIENTOS

Han sido tantas las cosas que he vivido desde que comencé mi carrera hasta ahora, tantas experiencias y personas las cuales han dejado una huella en mi vida y me han ayudado a convertirme en la mujer que soy hoy en dia. En primer lugar quiero agradecer a mi madre quien durante toda mi vida me ha brindado su apoyo incondicional y ha movido el mundo entero para ayudarme a cumplir mis sueños, a mi familia quienes siempre han creído en mí y han celebrado mis éxitos como si fueran también los suyos, a mi compañero de juventud, Claudio, quien me conoció cuando la idea de convertirme en astrónoma aún era algo muy lejano, le agradezco por la compania, amor y motivación que me entregó durante tantos años.

Un agradecimiento especial también a todos mis amigos y compañeros que he tenido durante mi paso por la universidad, gracias por su compañerismo y por ser en varias ocasiones mi segunda familia, gracias a mi amiga Camila, de quien escuche por primera vez el nombre de la Universidad de Concepción y con quien me aventuré a dejar nuestra ciudad natal por ir detrás del sueño de convertirnos en científicas.

Por último, quisiera dedicar estas últimas líneas a mis tutores de tesis, al profesor Ricardo por la oportunidad de trabajar con él y por confiar en que sí lograría sacar adelante este proyecto, al profesor Hector por su paciencia y disposición a enseñarme a pesar de la distancia, muchas gracias por su guía y cooperación.

Resumen

Se sabe que los núcleos activos de galaxias (AGN) son un ingrediente esencial en el proceso evolutivo de las galaxias, ya que están fuertemente asociados con el crecimiento de su agujero negro supermasivo central (SMBH) y el crecimiento de la masa estelar (es decir, la formación de estrellas). Además, muchos estudios muestran que el entorno local de las galaxias desempeña un papel importante en la conducción de los procesos por los que pueden perder o ganar gas, y por consiguiente afectar a la activación de sus núcleo. Por lo tanto, investigar cómo el medio ambiente puede influir en las propiedades observables del AGN puede contribuir a nuestra comprensión de la evolución de las galaxias. Los mejores laboratorios para estudiar el impacto del medio ambiente en las galaxias son los cúmulos de galaxias. Por consiguiente, esta tesis presenta un estudio espectroscópico de campo integral de dos AGN miembros del cúmulo de galaxias RXJ0152-137 con desplazamiento al rojo de z = 0,84. Los datos se obtuvieron usando el instrumento KMOS, un espectrómetro multi-objeto en el infrarrojo cercano (0,8 μm a 2,5 μm), que está montado en el telescopio UT1 del VLT ubicado en Cerro Paranal, Chile.

Para uno de los AGN de cúmulo, ID=557, se detectó la emisión de las líneas estrechas de Hα y [NII], así como la de una componente ancha desplazada al rojo para Hα con una velocidad de v = 938 $\pm$ 74 km s^{-1} con respecto a la componente estrecha. Sin embargo, para el otro AGN, ID=300, sólo fue posible detectar la componente ancha de Hα. Las líneas estrechas no fueron detectadas, siendo la ausencia de emisión de [NII] un posible indicador de la baja metalicidad de este AGN.

Realizamos un análisis cinemático del gas ionizado del AGN ID=557 construyendo los mapas de velocidad, dispersión de velocidades y distribución de flujo de las líneas de emisión óptica Hα y [NII]. Además, complementamos este análisis con un estudio fotométrico a partir de imágenes del HST para obtener una clasificación morfo-cinemática de este AGN. Encontramos que ambas galaxias corresponden a AGN tipo 1. Ademas, el AGN ID=557 puede ser clasificados como Pec/CK, es decir, una galaxia con morfología peculiar y una cinemática compleja con dos ejes cinemáticos. Finalmente, comparamos los resultados obtenidos para cada AGN según su ubicación dentro del cúmulo de galaxias. Discutimos la posible

conexión del entorno con las metalicidades inferidas para cada una de ellas, y la posible interacción del AGN ID=557 con una galaxia vecina no confirmada, que se observa en las imágenes del HST. Este trabajo muestra una clara evidencia de cómo los AGN del mismo tipo pueden mostrar diferencias en sus propiedades espectroscópicas dependiendo de la región del cúmulo en la que se desarrollan. Sin embargo, estos resultados deben ser complementados con el análisis de una muestra de más galaxias para tener una mejor representación de la población de galaxias del cúmulo. Es necesario utilizar IFS de mayor resolución para resolver de mejor manera sus cinemáticas internas, con el fin de comprender con más detalle los procesos físicos que afectan a las galaxias en los ambientes de cúmulos.

Abstract

It is known that active galaxy nuclei (AGN) are an essential ingredient in the evolutionary process of galaxies, since they are strongly associated with the growth of their central super massive black hole (SMBH) and stellar mass growth (i.e. star formation). Also, many studies show that the local environment of galaxies plays an important role in driving the processes by which they can lose or gain gas, and therefore affect the activation of their nucleus. Hence, investigating how the environment can influence the observable properties of AGN can contribute to our understanding of the evolution of galaxies. The best laboratories to study the impact of the environment on galaxies are galaxy clusters. Consequently, this thesis presents an integral field spectroscopic study of two members AGN of the galaxy cluster RXJ0152-137 at redshift z = 0.84. The data were obtained using the KMOS instrument, a multi-object near-infrared (0.8 μm to 2.5 μm) spectrometer, which is mounted on the UT1 telescope of the VLT located on Cerro Paranal, Chile.

For one of the cluster AGN, ID=557, the emission from the Hα and [NII] narrow lines was detected, as well as that from a broad redshifted component for Hα with a velocity of v = 938 $\pm$ 74 km s^{-1} concerning the narrow component. However, for the other AGN, ID=300, it was only possible to detect the broad component of Hα. The narrow lines were not detected, being the absence of [NII] emission a possible indication of the low metallicity of this AGN.

We performed a kinematical analysis of the ionized gas of AGN ID=557 by constructing the velocity, velocity dispersion, and flux distribution maps of the optical emission lines Hα and [NII]. Also, we complement this analysis with a photometric study from HST images to obtain a morpho-kinematic classification of this AGN. We found that both galaxies correspond to type 1 AGN. Besides, the AGN ID=557 can be classified as Pec/CK, that is, a galaxy with peculiar morphology and complex kinematics with two kinematic axes.

Finally, we compare the results obtained for each AGN according to their location within the galaxy cluster. We discuss the possible connection of the environment with the metallicities inferred for each of them, and the possible interaction of AGN ID=557 with an unconfirmed neighboring galaxy, which is observed in the HST images. This work shows evidence of how the same AGN type can show differences

in their spectroscopic properties depending on the region of the cluster in which they develop. However, these results must be complemented with an analysis of a larger sample of galaxies to have a better representation of the cluster's galaxy populations. We need to use higher-resolution IFS to better resolve their internal kinematics to understand in more detail the physical processes that affect galaxies in cluster environments.

Keywords – galaxies: active – galaxies: high-redshift – galaxies: kinematics and dynamics

Contents

List of Tables

List of Figures

Chapter 1

Introducción

1.1 Active Galactic Nuclei

Some galaxies in the Universe show unusual, very bright nuclear regions, characterized by energetic/non-stellar processes. These nuclei are called Active Galactic Nuclei (AGN) and their hosts are referred to as active galaxies. Currently, it is accepted that the AGN radiation is connected to the accretion onto a super massive black (SMHB) with mass $\geq 10^6 M_\odot$. The AGN include a wide range of different objects characterized by several properties:

a) **Very High luminosity:** These objects release a very large amount of energy evidenced by very high luminosities (up to $L_{bol} \sim 10^{48}$ erg s^{-1}) which makes them the most powerful sources in the Universe, and they have been observed up to very high redshift (z=7.54; Bañados et al. 2018).

b) **Large coverage of the electromagnetic spectrum:** AGN have been detected in all spectral ranges, and each wavelength band provides a window to observed different aspects of AGN physics. For example, the infrared band (IR) is sensitive to the dust and obscuring material, the optical/UV bands allow us to observe the emission from the central accretion disc through continuum emission and emission lines, while γ-ray and radio bands (corresponding to atomic and molecular gas) allow us to detect non-thermal radiation related to the observed lobes. Finally, with the X-ray band it is possible to trace the coronal emission.

c) **Strong emission lines:** AGN are characterized by the presence of strong nebular emission lines observed in the optical/UV spectral range (see figures 1.1.1 and 1.1.2). These lines are related to high ionization processes, and in some cases the line widths can extend from hundreds to thousands of km s^{-1}.

d) **Variability:** AGN are also characterized by a brightness variability in timescales of minutes, hours and even days or months depending on the spectral band.

1.1.1 AGN types

AGN comprise a heterogeneous group of objects resulting in a large variety of subtypes with different properties among them, such as the mass of the central black hole, bolometric luminosity ranges, and even in optical/UV emission lines where in some AGN spectra they appear highly marked, while in others they seem to be absent (see figures 1.1.1 and 1.1.2). The large number of differences discovered for AGN subtypes is mainly due to the nature of the emitted radiation observed in some spectral bands, so the main classification of these objects is on an observational basis. The following are some of the main subclasses of AGN:

1. **Seyfert Galaxies:**
   Seyfert galaxies were the first AGN identified by Seyfert (1943) and the most common subclass of AGN observed in the local Universe. The main difference between Seyfert galaxies and nonactive galaxies is the bright, central, point-like core observed in direct images. In addition, with the advent of large telescopes and advanced instrumentation it became possible to obtain the spectrum from the unresolved core and distinguish it host galaxy emission. The central optical spectra show highly ionized lines which can present broad and/or narrow components. Khachikian and Weedman (1974) separated the Seyfert galaxies into classes depending to the relative widths of narrow forbidden emission lines and Balmer lines observed in the optical spectra. These class of Seyfert galaxies, and others too, are present in the following paragraphs:

   - **Seyfert 1 (Type 1 AGN):** These galaxies display Balmer emission lines, mainly Hα, Hβ, and Hγ, broader than forbidden lines with full

width at half maximum (FWHM) $\sim$ 1,000-20,000 km s^{-1} (Netzer 2015). Narrow permitted and forbidden lines are also observed. Both low ionization lines and high ionization lines like [OIII]λ4959 Å and [OIII]λ5007 Å present broad and narrow components. Another indication of type 1 AGN is the presence of a strong Fe[II] line at 4,570 Å. An example of a Seyfert 1 spectrum is shown in figure 1.1.1.

- **Seyfert 2 (Type 2 AGN):** For these galaxies the forbidden and permitted emission lines to show the same narrow width of 300-1,000 km s^{-1} (Netzer 2015). The broad components are not detected. An example of a Seyfert galaxy is shown in figure 1.1.2.

  Also, there are intermediate classes of Seyfert galaxies, such as Seyfert 1.2, 1.5, 1.8, and 1.9, according to the presence of a broad Hβ Balmer emission following the outline proposed by Osterbrock (1981)

- **X-ray classification:** In the X-ray domain, another classification is established depending on the intrinsic absorption measurement in the soft X-ray band (E << 5 keV) where the absorption is measured as a column density of hydrogen N_H in the line of sight, in units of atoms per cm^2. Type 2 AGN are commonly the most strongly adsorbed sources, while type 1 present less absorption. The intermediate objects with $N_H < 10^{22}$ cm^{-2} have been classified as Seyfert 1 or Seyfert 1.2, whereas Seyfert galaxies with $N_H > 10^{22}$ cm^{-2} correspond to Seyfert 1.8, 1.9 or 2.

- **Narrow-Line Seyfert 1 Galaxies (NLS1):** This subset of Seyfert 1 galaxies are strong X-ray emitters with a clear difference between two Balmer lines: while Hα lines are broad, the Hβ lines are narrow (FWHM(Hβ) < 2,000 km s^{-1}).

Moreover, some spectroscopic measurements reveal AGN candidates corresponding to galaxies with emission line spectra similar to those of Seyfert 2 galaxies. This characteristic is often produced by massive gas clouds of ionized hydrogen known as HII regions. They are observed mostly in spiral and irregular galaxies, and also often show strong forbidden emission lines, such as oxygen, in comparison with Balmer lines, with [OIII] λ5007/Hβ > 3. To distinguish the correct classification for these gala.xies in necessary to

examine the ionization levels in more detail using various emission lines to reproduce some diagnostic diagrams such as that discussed in 1.1.2.

2. **LINER galaxies:** The low-ionization nuclear emission-line regions (LINER; Heckman 1980) are active galaxies with faint core luminosities and strong emission lines resulting from low ionized gas. They show similar proprieties that Seyfert 2 galaxies with expected line widths of 200-400 km s^{-1}. LINERs mark the low luminosity limit for galaxies classified as AGN. .

3. **Quasars:** They were discovered in the 60s (Shields 1999) with the development of radioastronomy. Then, with an optical observation of these objects, it was found that they presented optical properties similar to blue stars so that these galaxies were called *quasi-stellar objects*. The quasars are the most luminous AGN, therefore, are also the farthest observable objects in the Universe.

4. **Blazars:** This classification is a special subclass of quasars. The common model for observed blazar emission is that these sources are quasars in which a relativistic jet is pointing at or very close to the observer's line of sight (Urry and Padovani 1995). These peculiar objects are dominated by high variability. The blazars are also subdivided into BL Lac objects and Flat Spectrum Radio Quasars (FSRQ) where the latter are in turn divided into Optical Violent Variables (OVV) and Highly Polarized Quasars (HPQ). BL Lac objects are characterized by a lack of prominent features in the optical spectrum.

5. **Radio Galaxies** AGN show high luminosities in the radio bands where the central regions produce, for example, extended radio jets. The luminosity of this emission varies at some radio wavelengths, so another observational classification appears depending on the radio-to-optical flux ratio. Frequently, the comparative bands are the optical B-band and the flux at 5 GHz. Henceforth, the luminosity ratio $R = L_{5GHz}/L_B$ indicates where the galaxy presents more or less radio emission compared with optical emission. This classification divides AGN into *Radio-loud*, when $R \geq 10$, and *Radio-quiet*, when $R < 10$. However, there is no clear definition yet as radio detection depends, for example, on the sensitivity of the telescope. There are several restrictions for this classification, but all of the AGN subtypes shown above

can be classified into the following two groups:

- **Radio-Loud:** This type of galaxies is found in giant elliptical galaxies, and extended jets and lobes are observed in radio emission. They are produced by a synchrotron process due to relativistic electrons in the hot material. Within this classification, we find radio-loud quasars and blazars.
- **Radio-Quiet:** This type of galaxies does not show any large radio structures, and their sub-classification is defined, depending on their optical/UV spectral properties, as Seyfert or LINER galaxies.

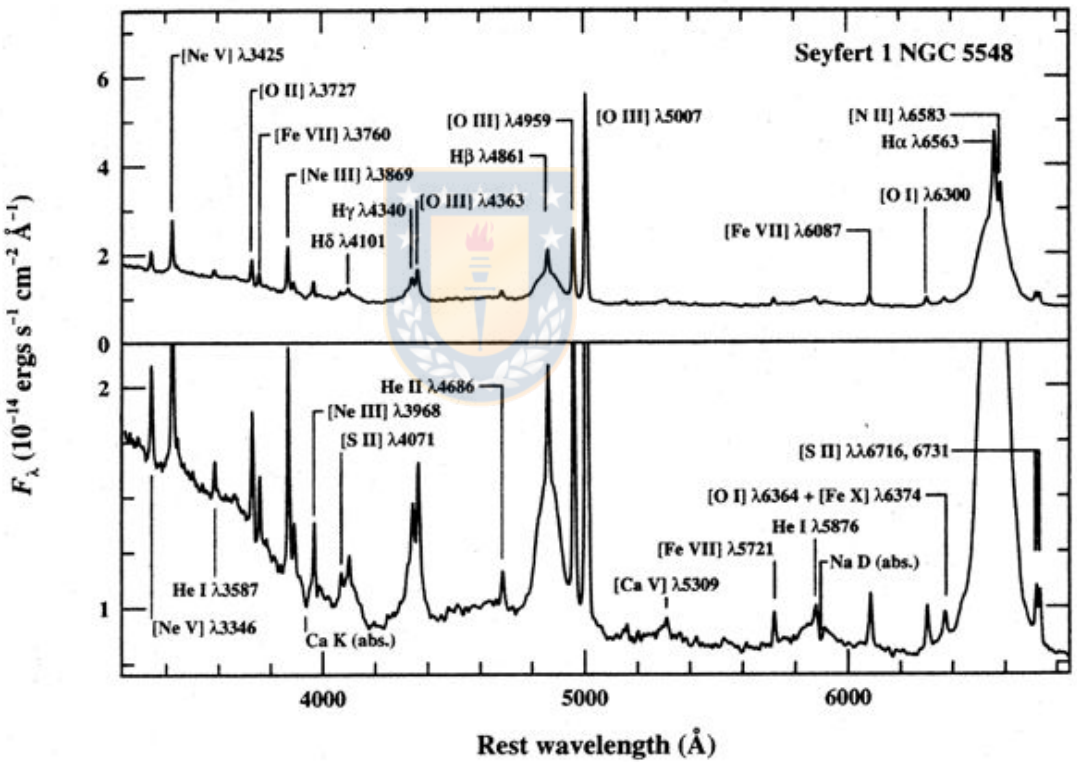

Figure 1.1.1: Example of a Seyfert 1 galaxy spectrum. It corresponds to the optical spectrum of the X-ray bright galaxy NGC5548 characterized by the broad Balmer lines Hα, Hβ, Hγ and Hδ, and narrow forbidden lines like [OIII], [OII] and [Ne III]. In the lower panel, the vertical scale is expanded to show the weaker features. This figure was taken from Peterson (1997).

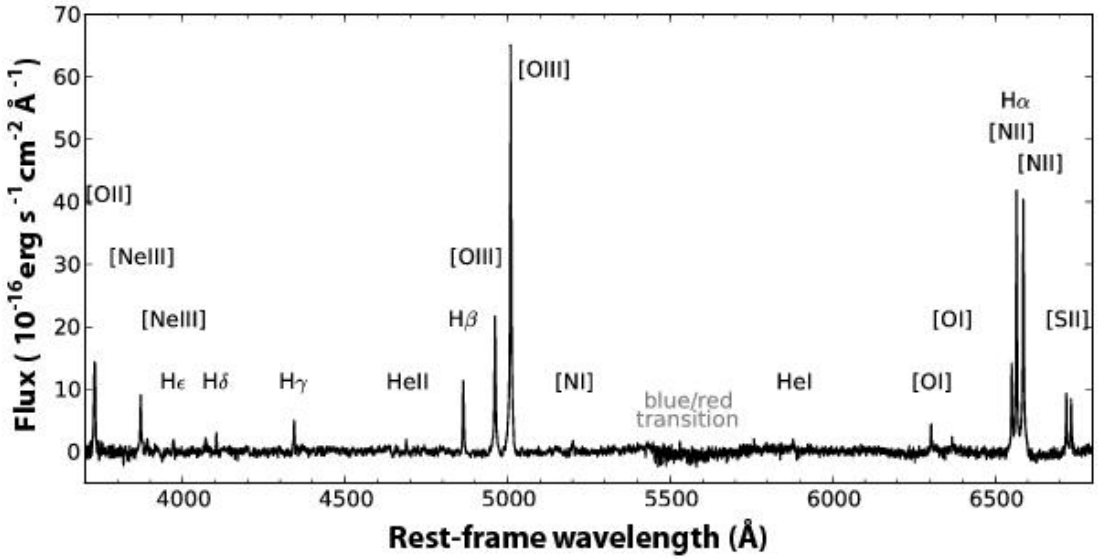

Figure 1.1.2: Example of a Seyfert 2 galaxy spectrum. This one corresponds to the nuclear spectrum of NGC 5427 presented by Dopita et al. (2014).

1.1.2 Emission lines

As previously mentioned, one of the most important characteristics of AGN spectra is the presence of strong optical/UV emission lines (see figures 1.1.1 and 1.1.2), which indicate the physical condition of the ionized gas, such as temperature, electron density, degree of ionization and metallicity. These lines are produced mostly through the photoionization of the gas in the nuclear region by the UV and X-ray emission from the AGN central engine, according to the photoionization model. The differences between them, cause that the AGN emission lines can be separated into two types coming from kinematically decoupled regions of the host galaxy. Hence, the two designations for these regions are the broad-line region (BLR) and the narrow-line region (NLR). The properties of each are described below.

- **Broad-line region:** From this region arise the so called *broad lines* which present full width at half maximum (FWHM) values from 1,000 km s^{-1} up to 20,000 km s^{-1}. Only permitted lines show broad components and the most prominent of these lines are the hydrogen Balmer series lines H$\alpha\lambda$6563 Å, H$\beta\lambda$4861 Å and H$\gamma\lambda$4340 Å. Also common are the Ly$\alpha\lambda$1216 Å, MgIIλ2798 Å, and CIVλ15449 Å lines. The BLR corresponds to high velocity clouds in regions close to the central engine assumed to be in photoionization equilibrium. The temperature of the BLR is the order of the 10^4 K which

means that the width of the broad emission lines cannot be produced only by thermal motion. This suggests the presence of another cause of broadening: the width of these lines is generally attributed to the Doppler effect due to the supersonic motions of each cloud around the dynamical center. Moreover, density values of $n_e \sim 10^9$ cm^{-3} indicate that in this region it is not possible to form forbidden emission lines. Therefore, this type of line is not observed in the BLR. According to the definitions of the AGN types mentioned above, the BLR is observed in Seyfert 1 galaxies, quasars, and broad-line radio galaxies. In figure 1.1.1, for example, it is possible to observe the Hα and Hβ broad emission lines from the BLR in the Seyfert 1 NGC5548 galaxy.

- **Narrow-line region:** From this region come the lines with FWHM $\sim 300 - 1,000$ km s^{-1} called *narrow lines*. The presence of forbidden as well as semiforbidden and permitted emission lines are indicative of gas densities $n_e \sim 10^3 - 10^5$ cm^{-3} and temperatures between 10,000 K and 25,000 K. The most important lines in this region are [OII]λ3727 Å, [OIII] $\lambda 4959, 5007$ Å, [NII] $\lambda 6548, 6583$ Å and [OI] $\lambda 6300, 6364$ Å. These. forbidden narrow lines are stronger than the permitted lines, especially [OIII]λ5007 Å. The NRL is a more extended region than the BLR, and is observed in all AGN types. However, in the case of Seyfert 2, LINERs galaxies and narrow-line radio galaxies only the NLR is observed. The BLR is not detected. In both figures 1.1.1 and 1.1.2, it is possible to observe the narrow emission lines originating from the NLR such as the Balmer emission lines and forbidden [OIII].

  Moreover, the relative flux of narrow lines is used to distinguish between HII regions, LINER, and Seyfert galaxies because these lines allow for the identification of high and low ionization processes. There are several diagnostic diagrams used to compare flux ratios of different lines to separate HII regions with a high ionization spectrum from AGN. Figure 1.1.3 shows an example of the most common pairs of flux ratios. The curves denote the limit between different galaxy classifications where the galaxies below the pure star-forming curve are classified as HII galaxies, those located in the area delimited by both curves are composite galaxies, while the AGN classification refers to galaxies above the extreme starburst curve. From the left panel in figure 1.1.3, the emission-line galaxies are distributed in a V-shaped area in the standard line ratio diagrams called a BPT diagram

(Baldwin et al. 1981), with the star-forming galaxies located in the left-hand branch and the AGN in the right-hand branch.

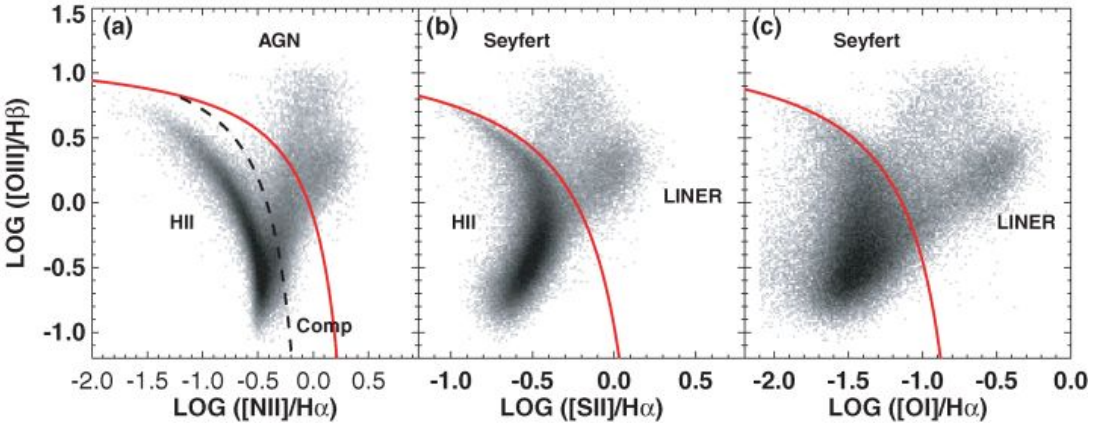

Figure 1.1.3: Diagnostic diagrams by Kewley et al. (2006). (a) [NII]/Hα vs [OIII]/Hβ, (b) [SII]/Hα vs [OIII]/Hβ, and (c) [OI]/Hα vs [OIII]/Hβ diagnostic for SDSS galaxies with S/N $>$ 3. The Kewley et al. (2001a) extreme starburst curve is shown as the solid red line, while the Kauffmann et al. (2003) pure star-forming curve is shown as a dashed black line. Galaxies located in the region between the two curves are classified as composite galaxies. Galaxies lying below the pure star-forming curve are HII galaxies, while those above correspond to AGN.

These flux ratios also allow us to infer some physical properties of the NLR such as the average ionization state and temperature of the photoionized gas through the [OIII]/Hβ flux ratio, and the metallicity commonly associated with the [NII]/Hα due to the nature of nitrogen as a secondary element. Consequently, the use of diagnostic diagrams is now also used to estimate the metallicity of the galaxies in question. Groves et al. (2006) used photoionization models to inspect the effects of metallicity variations on the narrow emission lines from an AGN sample. They found that line ratios involving [NII] are the most robust metallicity indicators in galaxies where the ionization comes from an AGN. This is observed in figure 1.1.4 where the modeled metallicity decreases when the [NII]/Hα ratio decreases. From the SDSS sample, they show that typical Seyfert NLRs have supersolar abundances, while low metallicity AGN ($Z < Z_{\odot}$) are very rare, with only $\sim$40 galaxies of the $\sim$23,000 Seyfert 2 galaxies from SDSS showing NLR abundances below solar values.

.

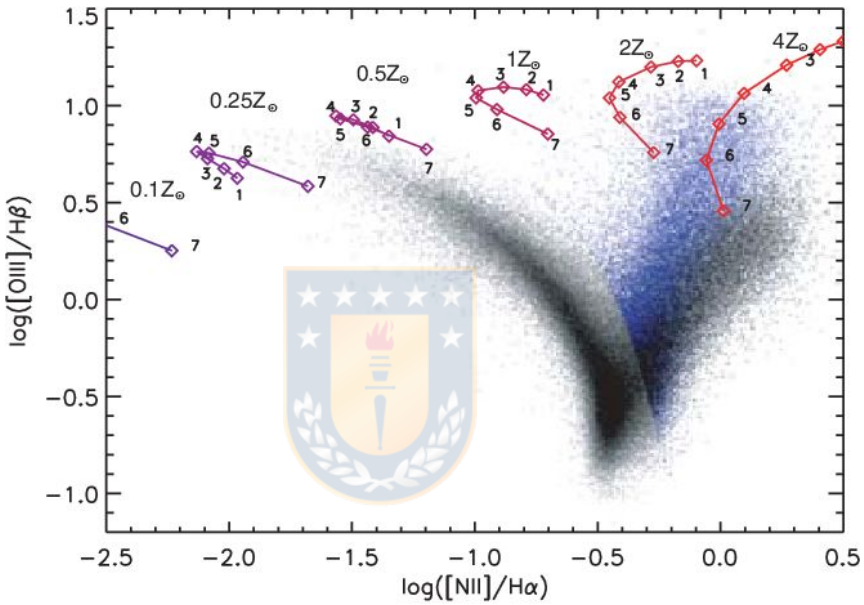

Figure 1.1.4: The BPT diagram of [NII]/Hα vs [OIII]/Hβ for the SDSS emission-line sample used to demonstrate the decrease of metal emission lines relative to hydrogen in the paper presented by Groves et al. (2006). The modeled metallicities are shown at the top of the figure, with the small numbers next to the model predictions indicating parameters associated with the model run and ionization parameter. The blue-coloured branch denotes the Seyfert galaxies in the SDSS sample.

1.1.3 The Central Engine

The special characteristics found for AGN suggest that the active galaxies host a source of energy added to the thermal source produced by the stars. Even though the different types of AGN show different proprieties, it is now widely accepted that all galaxies classified as AGN present the same physical phenomenon observed at different epochs. The most. accepted explanation is that AGN must be powered by accretion onto massive black holes at the center of their host galaxies.

Accretion of material onto a supermassive black hole (SMBH, $M > 10^6 M_\odot$) is an efficient way to produce the gravitational energy observed in the AGN since the energy released by material falling onto a central black hole is much larger than during the thermonuclear fusion of hydrogen (Lynden-Bell 1969). In this case, the material falls into the deep potential well of the black hole via a flat rotationally-supported disk, called the accretion disc, where the material loses its remaining angular momentum and falls onto the SMBH releasing the gravitational energy in the form of radiations or jets.

Moreover, there is currently solid evidence that supports the presence of an SMBH in the AGN. The problem is that black holes do not emit radiation that can be directly observed, so the presence is inferred through its interaction with the surrounding matter, such as monitoring the movement of stars around the black hole and observing how their trajectories can be modified by the central mass. However, the Event Horizon Telescope Collaboration and et al. (2019) was able to get the first image of a black hole, using a global very long baseline interferometry array. This allowed them to resolve the central compact radio source as well as an asymmetric brightness emission ring in the M87 galaxy.

1.1.4 AGN Unified Model

All the AGN types can be explained by a common underlying model which proposes that all of these objects correspond to the same physical phenomenon and the differences between them can be explained by orientation effects. The unified model (Urry and Padovani 1995) predicts that the anisotropy of the AGN population is caused by the difference levels of absorption of the radiation along the line of sight, consequently, the most general unification is based on the visible optical/UV emission lines (see table 2.1.3).

Moreover, figure 1.1.5 shows a representative scheme of the most current AGN unification model where the main different between AGN types is the presence or not of the jet emission, identified as radio-loud or radio-quiet AGN, respectively. Also, the visualization of the central. region is considered, which in some types of AGN is obscured by the torus.

Seyfert 1 and Seyfert 2 galaxies are then the same objects, seen from different angles. In the case of Seyfert 1, the nucleus and the accretion disk are observed nearly face-on, so it is possible to detect the emission from the NLR and also from the BLR. In Seyfert 2 galaxies the central part is obscured by the dusty torus that absorbs part of the optical/UV radiation, thus blocking the direct observation of the broad emission lines and attenuating the AGN continuum. .

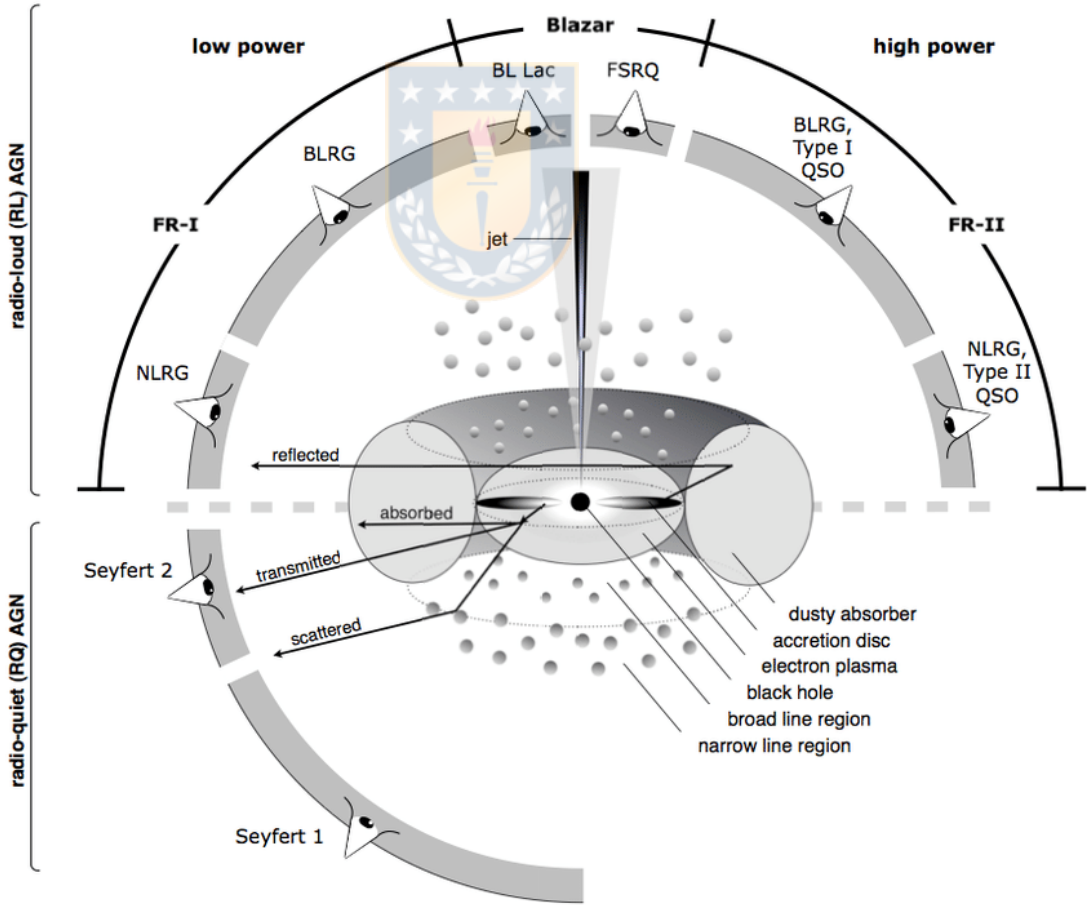

Figure 1.1.5: Scheme of the AGN unification model. The sub-types of AGN can be observed depending on the viewing angle. This model also distinguishes whether or not the AGN produces significant jet emission. Graphic by Marie-Luise Menzel in Beckmann and Shrader (2012).

Table 1.1.1: The general unification scheme of AGN, based on the emission lines visible in the optical domain. Information taken from book Beckmann and Shrader (2012).

Type	**Optical lines**	**Radio-quiet**	**Radio-loud**
Type 0	No lines	SgrA Dormant AGN[a]	BL, Lac, OVV
Type 1	Broad and narrow lines	Seyfert 1 Seyfert 1.5 NLS1	FSRQ, SSRQ,BLRG
Type 2	Narrow lines only Weak narrow lines	Seyfert 1.8,1.9,2 LINER/LLAGN	NLRG, type 2 QSO WLRG

[a] One might argue here that a dormant or nonactive AGN is indeed by definition not an AGN!

1.1.5 AGN in galaxy clusters

AGN are not isolated in the Universe. In that context, they can interact with objects and surrounding matter depending on the environment in which they develop. The best laboratories to study how the. environment can influence the features of AGN, and galaxies in general, are galaxy clusters. The processes that shape galaxy properties are expected to be more prominent in this type of environment due to the larger density of the intracluster medium (ICM), galaxies, and dark matter.

Galaxies in clusters are known to evolve faster from galaxies in low-density environments. This is evidenced by the significantly larger fraction of red elliptical galaxies than in the field, known as the morphology-density relation (Dressler 1980; Postman and Geller 1984; Postman et al. 2005; van der Wel et al. 2007; Holden et al. 2007; Mei et al. 2012; Bassett et al. 2013; Houghton 2015), and the fraction of star-forming cluster galaxies which increases strongly with redshift and also with ratio (Butcher and Oemler 1984; Ellingson et al. 2001). In density environments such as galaxy clusters, the galaxies can be influenced by several processes such as galaxy-galaxy mergers (Barnes and Hernquist 1991), ram-pressure stripping (Gunn and Gott 1972), galaxy harassment (Moore et al. 1996), evaporation by the hot ICM (Cowie and Songaila 1977), "strangulation"Larson et al. (1980), and others. These processes can hinder or facilitate the availability and transport of cold gas to the galaxy's center and therefore affect the AGN activity.

Studies have shown that the fraction .of cluster galaxies that host AGN is lower

than in the field (Dressler et al. 1985; Ehlert et al. 2014) but, the fraction of AGN seems to increase toward low clustercentric radii (Galametz et al. 2009; Martini et al. 2013). Also, there is a clear dependence on the frequency of AGN in galaxy clusters with redshift, where it increases with increasing redshift (Galametz et al. 2009; Pentericci et al. 2013; Martini et al. 2013; Bufanda et al. 2016). This is interpreted as evidence that the AGN population in clusters has evolved faster than the field population from at least z∼1.5 to the present (see Martini et al. 2013).

1.2 Galaxy Kinematics through Integral Field Spectroscopy

To understand in more detail the evolution of galaxies and the physical processes that occur within them it is important to know their structure, the distribution of their components such as gas, stars, etc, as well as their internal kinematics. However, for this, we need to be able to spatially resolve a galaxy. This is possible using the technique of Integral Field Spectroscopy (IFS) which consists of obtaining spectroscopic data of a certain field of view of an extended object by dividing it into sections as shown in figure 1.2.1, commonly called "spaxels". The light coming from each spaxel is received in a spectrograph equipped with an integral field unit (IFU) to then obtain a spectrum for each section of the galaxy. All the obtained spectra are organized in a data cube that contains the information of the field of view in 2D plus a third dimension that stores the spectral data.

There are different methods to perform this technique, which mainly differ in the way of splitting the field of view. The three main ones used in astronomy are a lens matrix, fibers, and an image slicer. The latter is shown as an example in figure 1.2.1, where the image of an object hits the mirror matrix that dissects it and sends it to different channels. Then each cut is re-printed on a slit by a pupil mirror and then is represented along a pseudo-slit row with the dissection in the spatial dimension happening through the detector pixels similar to what occurs in a classical long-slit spectrograph.

IFS studies with the first generation of instruments such as SINFONI (**?**) at the Very Large Telescope (VLT) have been very relevant to understand the internal processes that trigger the early growth of massive galaxies (Genzel et al. 2006;

Förster Schreiber et al. 2006; 2009; Shapiro et al. 2008; Förster Schreiber et al. 2018; Davies et al. 2019). Regarding the study of AGN, IFS through SINFONI and the new second generation of instruments such as the Multi-Unit Spectroscopic Explorer (MUSE; Bacon et al. 2010) and the K-band Multi Object Spectrograph (KMOS; Sharples et al. 2004; Sharples et al. 2013) has promoted a great advance in the analysis of these objects since it has allowed to spatially solve the structure, extension and kinematics of AGN outflows (Riffel et al. 2013; Collet et al. 2016; Harrison et al. 2016; Radovich et al. 2019; Davies et al. 2020). With these new advanced instruments it is now possible to efficiently obtain large samples of near-infrared IFS data where, for example, KMOS is ideal for systematic studies of the rest-frame optical properties of high-redshift galaxies and AGN (Harrison et al. 2016; 2017; Stott et al. 2016; Wisnioski et al. 2015; 2019).

Rodrigues et al. (2016) studied a representative sample of intermediate-mass galaxies at z∼1 from the KMOS^{3D} survey (Wisnioski et al. 2015; 2019) in order to define a methodology that can robustly identify virialized and isolated disks of galaxies involved in a merging sequence. They combined kinematic results with morphological analyses of HST images to define a complete morpho-kinematic classification of these galaxies.

1.2.1 The KMOS instrument

The K-band Multi-Object Spectrograph (KMOS; Sharples et al. 2013) is a second-generation instrument implemented on the Unit Telescope 1 (UT1) of the VLT in Cerro Paranal, Chile. It consists of a spectrograph qualified to perform integral field spectroscopy in onear-infrared bands of 24 objects simultaneously.

It is composed of 24 arms that can be positioned to cover a field of 7.2 arcmins. Each arm is an IFU with a field of view of 2.8″ x 2.8″ and a sampling of 0.2″ per pixel, maintaining the Nyquist sampling (≈2 pixel) of the spectral resolution element in the detector.

KMOS implements the image slicer method to divide the field of view of an object. The targets selected for observation are distributed among the 24 IFUs which divide each object into 14 identical slices, with 14 spaxels along with each slice. The light entered into the IFUs is then scattered by three cryogenic grid spectrometers that generate 14x14 spectra with 1,000 Nyquist-resolution elements

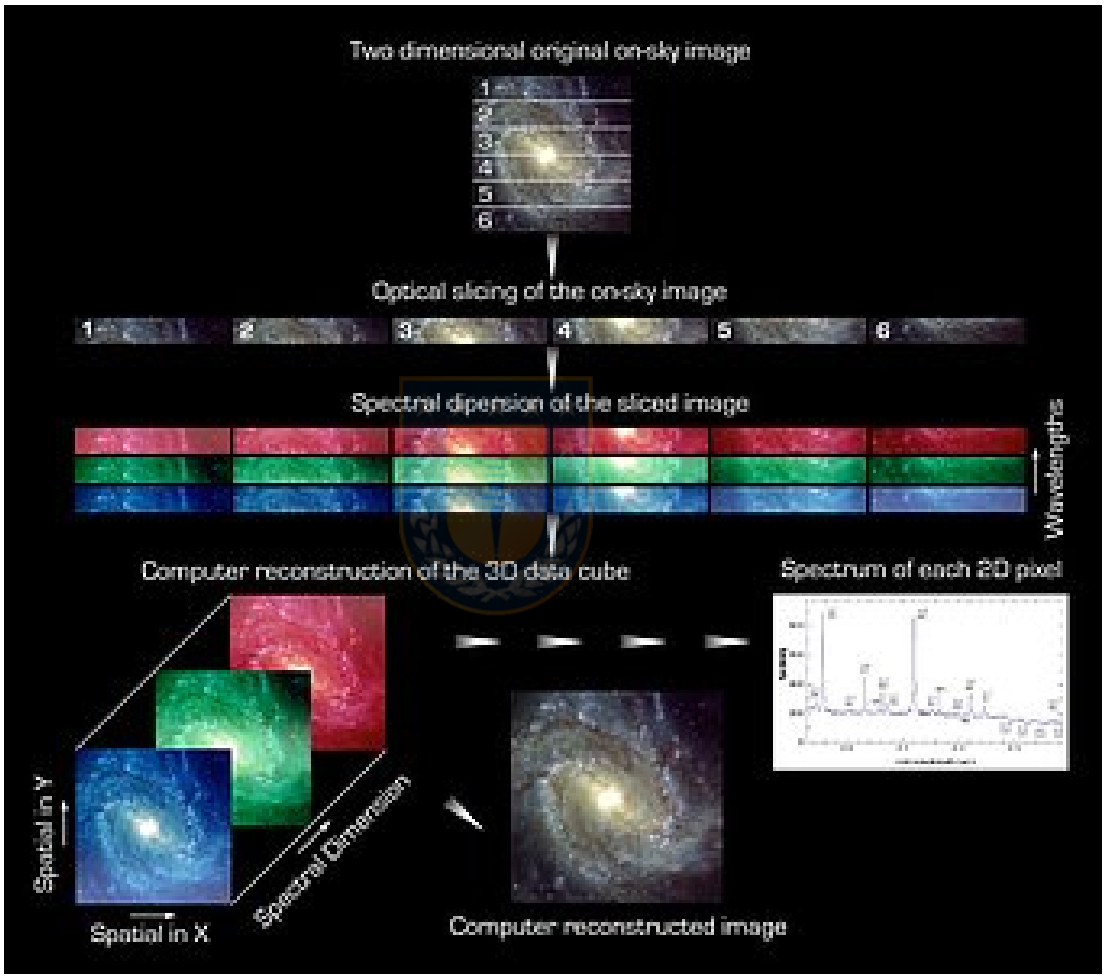

Figure 1.2.1: Illustration of how integral field spectroscopy works through the image slicer method. From ESO KMOS User Manual (https://www.eso.org/sci/facilities/paranal/instruments/kmos/doc.html).

sampling each of the 24 independent objects.

The main technical specifications of KMOS are shown in the table 1.2.1. o

Table 1.2.1: Summary of KMOS technical specifications.

Wavelength coverage	0.8 μm to 2.5 μm
Spectral bands	IZ, YJ, H, K, HK
Spectral resolving power	R = 3400, 3600, 4000, 4200, 2000 (IZ, YJ, H, K, HK)
Number of IFUs o heightExtent of each IFU	24 2.8" x 2.8"
Spatial sampling	0.2" x 0.2"
Patrol field	7.2 arcmin diameter circle
Closest approach of IFUs	$\leq$ 2 IFUs separated by $\approx$6 arcsec centre to centre of the IFU, depending on the details of the configuration.

From the hardware perspective, the instrument is divided into the following subsystems:

- Pick-off subsystem
- IFU subsystem
- Spectrograph subsystem
- Detector subsystem
- Infrastructure subsystems and electronics

Figure 1.2.2 shows a visual scheme of how this whole set of KMOS instrument subsystems is mounted on the Nasmyth platform of the VLT UT1. The mechanical parts of the instrument are all contained within a cryostat, which is operated at a temperature of 120 K, while the electronics are in the Nasmyth platform and inside the cable rotator. On the other hand, the pick-off system of the instrument arms is shown in figure 1.2.3.

The specifications of the KMOS detector are shown in the table 1.2.2.

Table 1.2.2: Characteristics of the KMOS detectors.

Detector type Operating temperature	Substrate removed Hawaii 2RG 35 K
QE	>90 %
Number of pixels	2048 x 2048
Pixel size	18 m
Gain (e - /ADU)	2.08
Readout noise (e)	9 for short DIT 2.6 for long integration with Fowler sampling
Saturation (ADU)	>60,000 ADU
Non-linearity o heightPersistence	>55,000 ADU >5,000 ADU
Hot pixels	≈1% in detectors 2 and 3; ≈3% in detector 1
Minimum DIT (s)	2.47

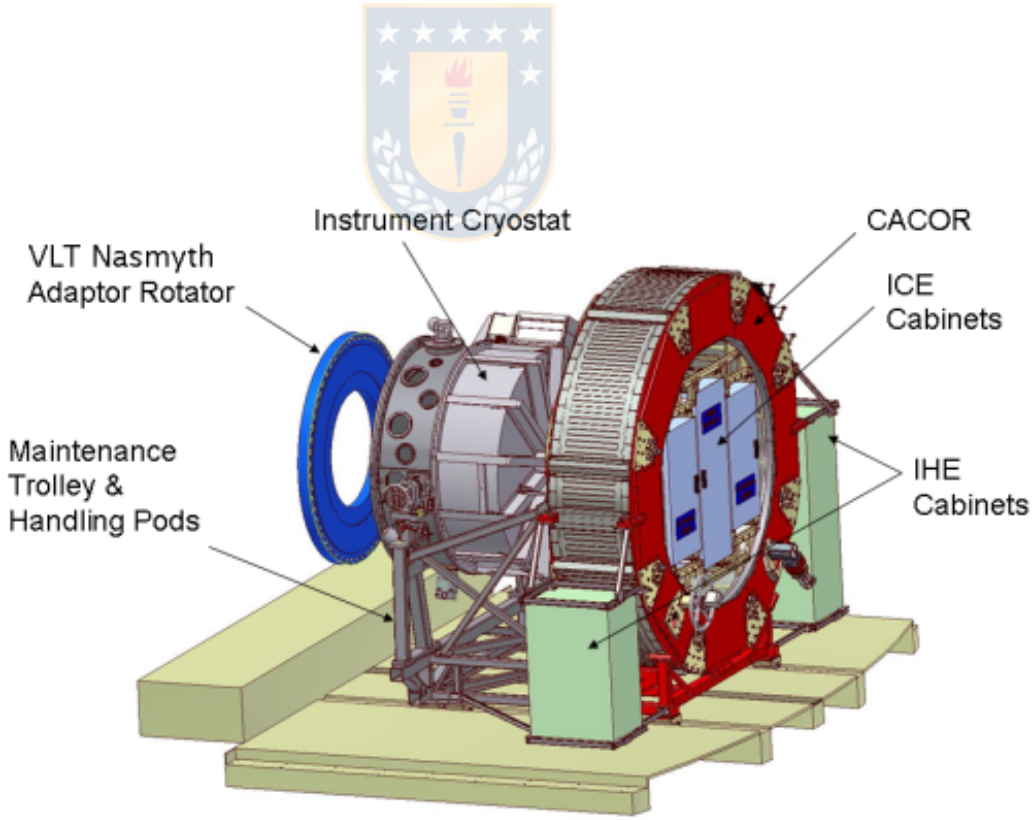

Figure 1.2.2: Schematic view of KMOS on the Nasmyth platform. From ESO KMOS User Manual (https://www.eso.org/sci/facilities/paranal/instruments/kmos/doc.html).

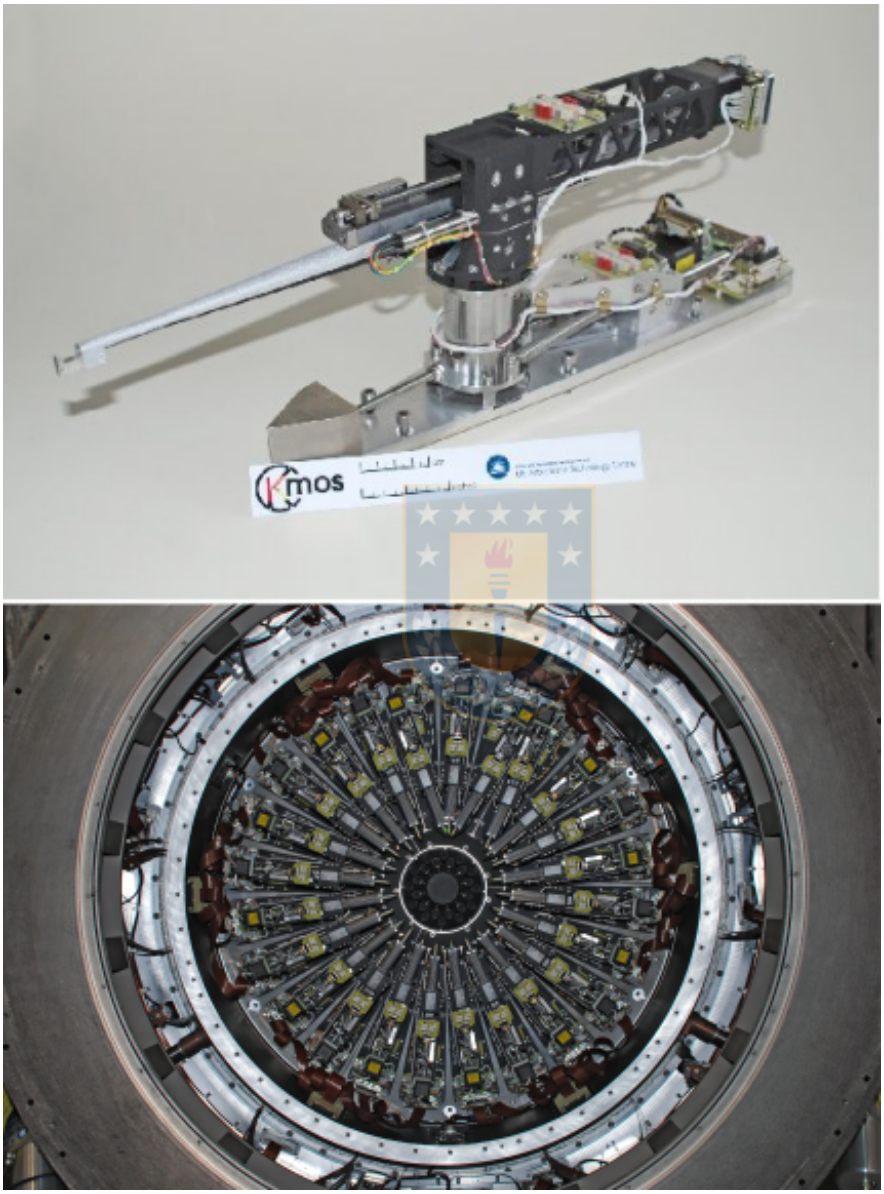

Figure 1.2.3: Top: one of the pick-off arms; Bottom: all the 24 pick-off arms in the front end of the KMOS cryostat. From ESO KMOS User Manual (https://www.eso.org/sci/facilities/paranal/instruments/kmos/doc.html).

1.3 This research

There is evidence of co-evolution between the growth of SMHBs and the star formation in galaxies (Alexander and Hickox 2012; Kormendy and Ho 2013). For example, one of the most direct results of this connection is that AGN and the star formation rate in galaxies show a similar cosmic evolution from z $\sim$ 2 to the present (Franceschini et al. 1999; Kauffmann et al. 2003; Merloni et al. 2004; Madau and Dickinson 2014; Aird et al. 2015). Any mechanism that enables the input of cold gas in a galaxy has the potential to trigger star formation as well as AGN activity. Then, it is thought that AGN feedback can regulate star formation, stripping the galaxy off of the necessary conditions as the cold gas (Fabian 2012; Somerville and Davé 2015), for which it is assumed that AGN are a phase of galaxy evolution. Therefore, studying AGN can contribute to understanding the evolution of galaxies.

As previously mentioned in section 1.1.5, AGN can experience a series of processes associated with the environment during their path through a galaxy cluster. Thus, analyzing the properties of these galaxies in this type of environment becomes very relevant to the study of how galaxies evolve.

In this thesis, the integral field spectroscopy analisys of two Type 1 AGN in a galaxy cluster are presented. As discussed in section 1.2, IFS data are necessary to spatially resolve the internal kinematics of galaxies. Therefore, by using data obtained with the KMOS instrument at the VLT, we can analyze the structure and complex kinematics of the ionized gas in galaxies. Thus, we can study the blended emission from the NLR by optical emission lines detected in the KMOS wavelength range. Besides, we complemented the spectroscopic data with photometric information from HST/ACS images.

Although we cannot make any definite conclusions about how the galaxy cluster environment affects the properties of AGN, we found important differences between the two AGN studied that allow us to discuss the possible relation with the influence of the environment in these two galaxies. Also, we focus the study on finding galaxies in the local universe with properties similar to one of our AGN, ID=557 assuming that distant galaxies can be classified with the same scheme as that used for local galaxies, in terms of dynamic and morphological properties.

In the following, Chapter 2 describes the observation process and subsequent data reduction implemented for the KMOS data cubes. The data analysis and the results are described in detail in Chapter 3. This includes emission line profile fitting, construction of velocity and velocity dispersion maps, photometric analysis, and morpho-kinematic analysis. Finally, in Chapter 4 we discuss the results for each galaxy in the context of identifying differences that may be indicators of the environmental influence. Throughout this manuscript, we adopt $H_0 = 70$ km s^{-1} Mpc^{-1}, $\Omega_M = 0.3$ and $\Omega_\Lambda = 0.7$.

Chapter 2

Observation and Data Reduction

2.1 Observation

The data used for this project were obtained with the KMOS instrument at the VLT as part of 4 observational programs (PI R. Demarco) between the years 2013 and 2016. These are the ESO programs ID = 092.A-0868, 093.A-0834, 096.A-0171 and 098.A-0380. The main aim of the programs was to better study and understand the effect of the cluster environment (particularly the driver of quenching) on the observed properties of cluster members. This was done by analyzing the internal kinematics of galaxies. Considering technical limitations, this was only possible for galaxies with emission lines in their spectra, i.e. star-forming galaxies. Ideally, one would like to do this study from absorption lines as well, but this may have to wait for larger telescopes such as the E-ELT.

The sample of galaxies was selected from 6 galaxy clusters where the [OII] emission was used as a proxy for Hα emission so were selected star-forming galaxies with [OII] emission lines based on the identification provided in Demarco et al. (2005; 2010). Table 2.1.1 shows in detail the characteristics of the clusters and the number of galaxies observed from each one. Depending on the redshift of each cluster, the required lines are detectable within the wavelength range of the KMOS YJ and H bands.

In the 4 programs the data were obtained in the nod-to-sky mode with an object-sky observation sequence of AB AB, that is, one sky observation for each object observation. Table 2.1.2 specifies the clusters that were observed in each program

Table 2.1.1: Clusters description and the number of galaxies observed in each one using two of the bands of the KMOS instrument of the VLT.

Target	RA	DEC	z	Band	n^o galaxies
RXJ0152-1357	01:52:44	-13:59:01	0.84	YJ	31
XMMUJ1229+0151	12:29:32	+01:52:16	0.97	YJ	18
RDCSJ1252-2927	12:52:57	-29:28:07	1.24	H	21
XMMUJ2235-2557	22:35:21	-25:57:40	1.39	H	21
XMMJ2215-1738	22:15:58	-17:37:58	1.46	H	21
CIGJJ0218.3-0510	02:18:20	-05:09:56	1.62	H	21

and the date when the observation was performed.

Table 2.1.2: Observation programs IDs and their respective dates of execution.

Program ID	Observation period	Clusters Observed
092.A-0868	2013-2014	RXJ0152-1357 XMMJ2215-1738 CIGJJ0218.3-0510
093.A-0834	2014-2015	XMMUJ2235-2557 XMMUJ1229+0151 RDCSJ1252-2927
096.A-0171	2015,visitor mode	RXJ0152-1357
098.A-0380	2016	RXJ0152-1357

From the total sample of 131 observed galaxies, two of these correspond to AGN selected for their intrinsic high scientific value with the aim of better understand the role of the environment in triggering AGN activity is. These AGN were previously discovered on Chandra observations of the cluster (Maughan et al. 2003; Demarco et al. 2005). In this investigation, we only worked with these two AGN which are members of the RXJ0152-1357 cluster. This is because they present a high signal-to-noise detection of their lines compared with the rest of the sample and provides an important insight into how the environment of clusters may (or may not) influence the AGN activity. Table 2.1.3 shows the main characteristics of these two sources.

In total, the observations of both AGN included 5 nights of observation dated 2013-10-02, 2014-12-21, 2015-10-30, and 2016-10-12, collecting a total of 11 data-sets with an exposure time of 600 seconds for science objects in the YJ band with a spectral coverage of 1.01 μm - 1.35 μm and a typical resolving power of R$\sim$ 3,600. Since the seeing is usually reported for the optical band, specifically at 500

Table 2.1.3: Cluster members observed using KMOS/VLT. X-ray fluxes and luminosities previously obtained by Chandra observations are shown. Parameter information provided by Demarco et al. (2005). Fuxes are in units of 10^{-14} erg s^{-1} cm^{-2} and luminosities in units of 10^{44} erg s^{-1}.

ID	RA	DEC	f_x [0.5-2] keV	L_x [0.5-2] keV	f_x [2-10] keV	L_x [2-10] keV	z
300	01:52:43.792	-13:59:01.10	3.5097	1.0540	3.5989	1.2777	0.8201
557	01:52:39.836	-13:57:40.80	1.6961	0.1529	7.6439	1.9623	0.8672

nm, the seeing conditions under which the images were taken should have been corrected for the YJ band using the $\Delta\theta = \lambda^{-1/5}$ conversion. With that, the 11 data sets were obtained under seeing conditions between 0.45″ and 1.18″.

2.2 Data Reduction

The data reduction was performed using the ESOREX pipeline, a series of commands written especially for VLT data reduction. This pipeline has the advantage of being an interactive tool that allows the user to manually control the reduction tasks execution from the terminal command line which makes it easier to handle the input and output parameters in each reduction step. The steps are:

1. Dark correction
2. Flat correction
3. Wavelength calibration
4. Illumination correction
5. Telluric correction
6. Science reduction: sky subtraction and cube reconstruction.

For the last step of the reduction, we use the SKYTWEAK option for the subtraction of the skylines as this delivers final buckets with a lower contribution of subtraction waste compared to the default pipeline option. SKYTWEAK constructs synthetic cubes for the skylines through a spectral scaling of the individual OH line families to match the data (Davies et al. 2013). Also, to obtain the final cubes for each galaxy we combined all the individual observations performed to increase the signal-to-noise from the data.

A total of 131 data cubes were obtained. However, after a visual inspection of each cube, it was determined that for only two of the sources was it possible to detected the emission lines directly in the spatial image and in the spectral dimension of each spaxel. This is because the spectra are still contaminated with skyline residues even after performing the sky subtraction with the most efficient option. This contamination is due to the strong emission of vibrational-rotational transition lines resulting from non-thermal excitation processes of the OH molecule in the wavelength range of the near-infrared.

To clean the cubes of these residuals it was necessary to create a code written in the python programming language that involved:

- Identify in the science spectrum emission peaks which can be sky subtraction residuals.
- Differentiate between sky residuals and noise in the spectrum. For this, a sigma clipping analysis was performed on the spectral data to select only the peaks that are above the noise threshold.
- Identify and create a mask with the spectral pixels where the skylines are detected, this was done by comparing the positions of each line in the sky spectrum delivered by the reduction with the science spectra of each source considering a width of 5 pixels for the skylines (measured from the sky spectrum)
- Remove spectral pixels with sky residuals for each spaxel of the cube.

The result of the implementation of this method in the galaxy ID=557 is shown in the figure 2.2.1. At the top of the figure is shown the science spectrum as delivered by the pipeline, i.e. with the sky residues, while on the middle is shown the spectrum with the sky residues (red) masked, and finally, the bottom part shows the final spectrum with the removed residues. In all images, the vertical black lines at the top show the position of the OH lines in the whole spectrum range.

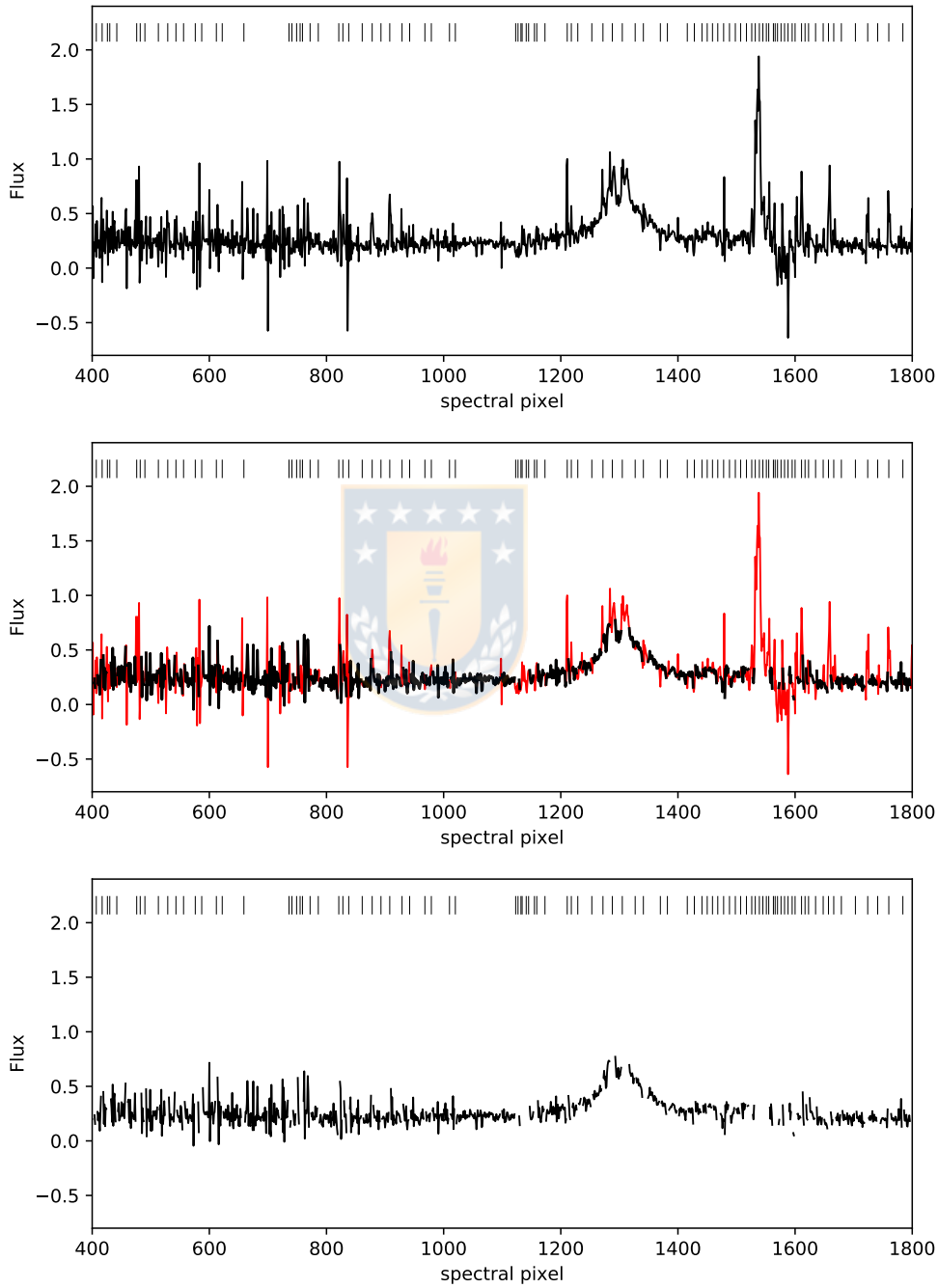

Figure 2.2.1: From top to bottom: the original integrated spectrum of galaxy ID=557 with sky residuals, the integrated spectrum (black) with the masked residuals (red), the final spectrum with the removed residuals. The black vertical lines show the position of OH skylines.

Chapter 3

Data Analysis

3.1 Emission line fitting

To begin with the analysis of the data cubes we first performed a spectral cut from 1.18 μm to 1.26 μm for AGN ID=557 and from 1.14 μm to 1.23 μm for AGN ID=300 to limit the spectrum to the range of line detection wavelengths. Then, we proceeded to fit and subtract the continuum emission of the galaxies to obtain only the contribution of the emission lines. For this, we measured the continuum level in two emission line-free windows around the detected emission in the integrated spectrum using the LMFIT package which is based on and extends many of the optimization methods of scipy.optimize and then we apply the method to all the spaxels in the cube with the Spectral-cube package from Python (Astropy Collaboration et al. 2013; 2018). Figure 3.1.1 shows an example of the fitting and subsequent subtraction applied to the galaxy ID=557.

Subsequently, we proceeded to fit the emission line profiles to obtain the flux, central wavelength, and wavelength dispersion parameters. Based on the redshift of each galaxy, the wavelength range of the KMOS YJ band, and a visual inspection of the spectrum, we observed that the detected emission lines correspond to H$\alpha\lambda$6563 Å and the [NII]λ6548, 6583 Å doublet.

To perform the fitting to each spaxel we first carry out a general inspection of the integrated spectra of the central region of the data cube to know the type of fitting required. After a visual inspection of the residues and the emission shape we determined to perform a multiple Gaussian fitting, one Gaussian for

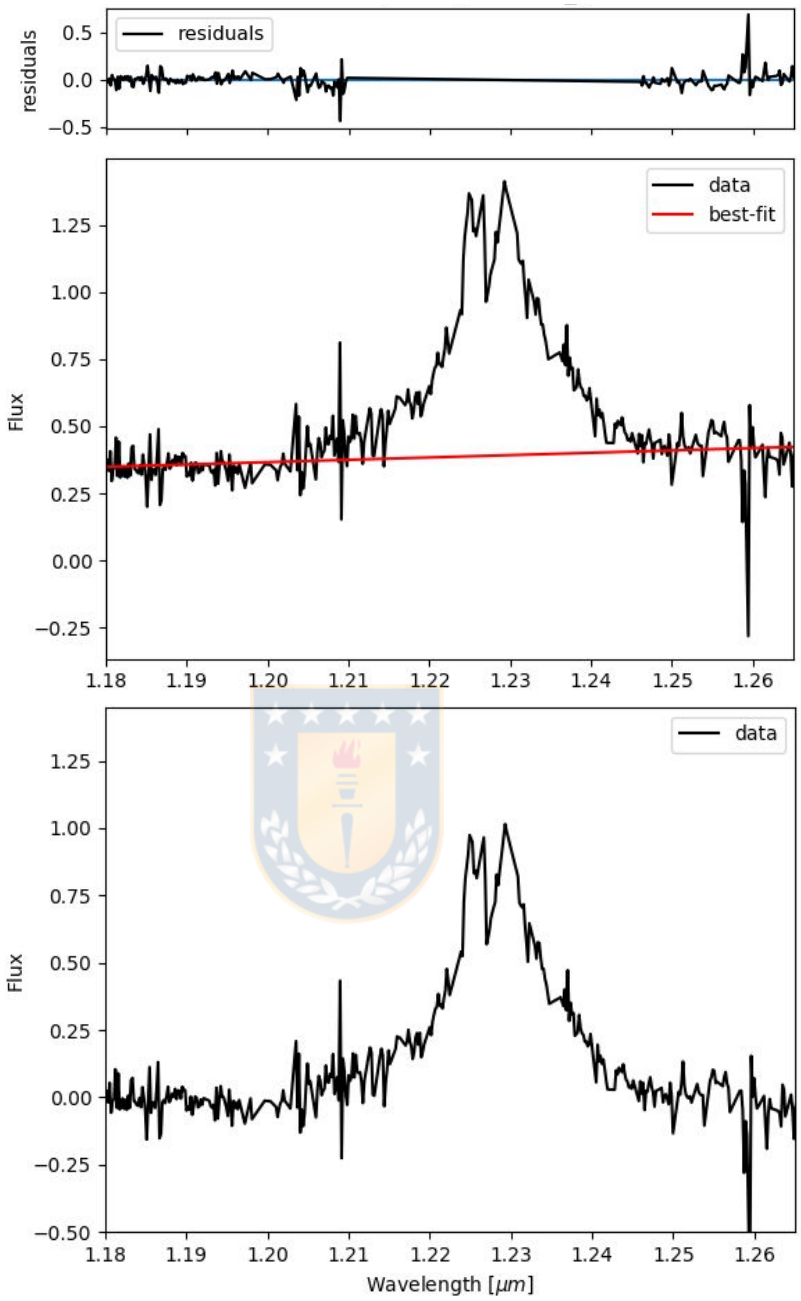

Figure 3.1.1: Fitting and subsequent subtraction of continuum level for the spectrum of galaxy ID=557 performed with the Python LMFIT package. From top to bottom: the fitting residues, the best fit to the continuum data shown in red and the final spectrum without the continuum emission.

each emission line detected.

For each spectrum, we tried a two Gaussian component fitting for the Hα emission line, with one narrow and one broad component. Besides, we fit two other Gaussian profiles to each line of the [NII] doublet, considering a relation between them that

is equal to the theoretical relation of 1:3 (Osterbrock 1981), together with the same value in dispersion since they correspond to lines that must come from the same region of the galaxy. For the case of the narrow line emission of Hα and [NII], we tested two possibilities, a fit in which all the narrow components have the same width and another in which their widths are different, assuming with the latter that the emission of Hα and [NII] come from different regions of the galaxy. Finally to choose one of the two possibilities we select the fit with the lowest value of χ^2, being the different dispersion option the best fit for narrow lines.

On the other hand, when fitting the broad component of Hα we assumed in the first instance that it should be centered on the same wavelength of its narrow component, however, as described below, for the case of the galaxy ID=557 this is not the best fit.

3.1.0.1 AGN ID=557 emission profiles

For this galaxy the narrow emission lines of Hα and [NII] were detected as well as a broad component for Hα, however, it was not possible to fit this last component to the same central wavelength of the narrow component. In this case, we found a broad component that is redshifted concerning the center of the narrow line of Hα as shown in the figure 3.1.2 where we measure a z = 0.8730 $\pm$ 0.0005 and a redshifted velocity of v = 938 $\pm$ 74 km s^{-1} for that component.

This type of AGN spectra was also found in low redshift AGN (z<0.37) by Zhang et al. (2009) in a sample of galaxies selected from the SDSS DR4 (Adelman-McCarthy et al. 2006). In their paper they propose a model where the appearance of a broad blue/red-shifted component in low-ionization lines such as Hα can be explained as the partial obscuration of the broad emission line region (BLR) in an AGN with double-peaked low-ionization broad emission lines also called dbp-emitters. To explain the two emission peaks, this model considers the presence of an accretion disk where the broad line emission comes from disk-like BLR moving in the accretion disk around the BH. In the unified model this disk-like BLR can be obscured by the torus (Antonucci 1993; Urry and Padovani 1995), making that in the optical spectrum of these AGN only one of the components to be detected, blue or red-shifted depending on parameters of the galaxy such as its inclination to our line of sight and the orientation angle of the disk-like BLR on

the accretion disk.

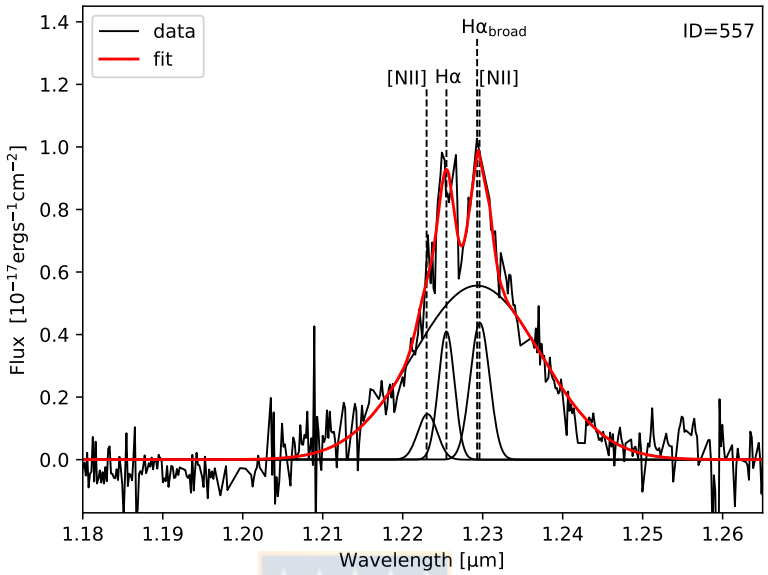

Figure 3.1.2: Integrated spectrum of the AGN ID=557 from the galaxy cluster RXJ0152-137 obtained with the KMOS instrument at the VLT. The black curves show the Gaussian components fitted to each emission line. The thin vertical black dashed lines indicate their centers. A redshifted broad component of Hα (H$\alpha_{\rm broad}$) is detected, with a redshifted velocity of v = 938 $\pm$ 74 km s^{-1}. The red solid curve shows the best multi-Gaussian fit found for this galaxy using the Python LMFIT package.

3.1.0.2 AGN ID=300 emission profiles

For this galaxy the same procedure of multi-Gaussian fitting was adopted in the first instance, however, the fit with the least value of χ^2 indicated that the narrow lines for Hα and [NII] were not detected. Therefore, as it is shown in the figure 3.1.3, only the emission corresponding to the broad component of Hα was observed which, unlike galaxy ID=557, is centered on the wavelength where the narrow Hα emission would be expected. The parameters found with the best fit for each emission line in both AGN are presented in the table 3.1.1.

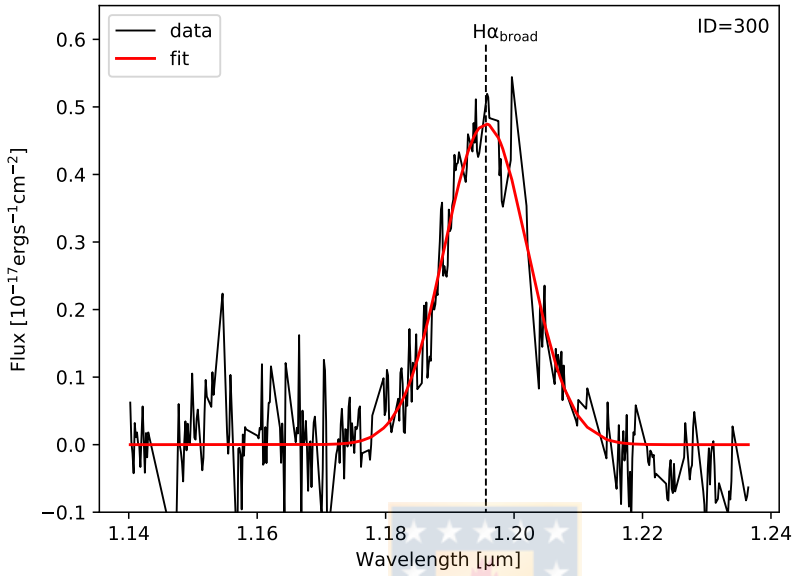

Figure 3.1.3: Integrated spectrum of the AGN ID=300 from the galaxy cluster RXJ0152-137 obtained with the KMOS instrument at the VLT. For this galaxy, it was possible to detect only the broad component of Hα. The black dashed line shows the wavelength position where the line was detected at which, contrary to ID=557, coincides with the wavelength at which Hα should be detected at z=0.8201.

Table 3.1.1: Emission Lines parameters for each source.

Source	Line	λ_0 [Å]	λ_{obs} [Å]	FWHM [km s^{-1}]	FLUX [10^{-17}ergs^{-1}cm^{-2}]	Reduced χ^2
ID=557	[NII]	6,548	12,230 ± 1	694 ± 90	2.52 ± 0.50	0.007521
	Hα_{narrow}	6,563	12,254 ± 1	571 ± 66	5.88 ± 1.17	
	Hα_{broad}	6,563	12,293 ± 2	4,572 ± 179	63.33 ± 12.67	
	[NII]	6,584	12,296 ± 1	690 ± 90	7.58 ± 1.51	
ID=300	Hα_{broad}	6,563	11,956 ± 1	3,865 ± 101	44.42 ± 8.89	0.002873

3.2 Kinematical mapping

To perform a spatial kinematic analysis of both AGN we proceeded to study each spaxel of the data cubes. First, we fit the emission line profile following the methodology described in section 3.1 in each AGN to measure the flux, central wavelength, and dispersion parameters for each emission to construct the flux distribution maps, velocity, and velocity dispersion maps.

After the fitting, we estimate the signal-to-noise ratio (S/N) of each line using the method described by Flores et al. (2006). However, for the case of galaxy ID=557, we extend the method to a multi-Gaussian fitting. In this method, the S/N corresponds to the ratio between the total flux in an emission line and the noise in the spectrum normalized by the number of spectral resolution elements in the wavelength range where the line was detected. To measure the noise we simply calculate the dispersion of the data in emission line-free windows, one on each side of the Hα and [NII] emission, in the same region where we have previously fitted the level of the continuum. Then we apply the following equation for each emission line:

$$\mathrm{S/N} = \frac{\sum_{\mathrm{i}}^{\mathrm{N}} \mathrm{S_i}}{\sqrt{(\mathrm{N})} \times \sigma} \tag{3.2.1}$$

where $\mathrm{S_i}$ corresponds to the flux in the spectral pixel i, N is the number of spectral resolution elements which for this case is about half of the total number of pixels where the line is detected, and σ the dispersion of the continuum (Flores et al. 2006). We select only spaxels that satisfy S/N > 5 for all emission lines.

The KMOS field of view is split into 196 spaxels in total as shown in figure 3.2.1, from which only 18 of them satisfy the restriction in S/N for galaxy ID=557. In the case of the AGN with multiple emission lines, even though both [NII] lines were detected, we cannot find spaxels with a S/N > 5 for [NII]λ6548 Å. Therefore, only [NII]λ6583 Å was considered for the kinematic analysis.

On the other hand, the KMOS data present an FWHM of the seeing disk of $\sim 0.6''$, which does not allow us to spatially resolve the broad emission lines. The size of the BLR is less than 100 pc (Peterson 1997), therefore, the emission from this region can be considered as the emission of a point object.

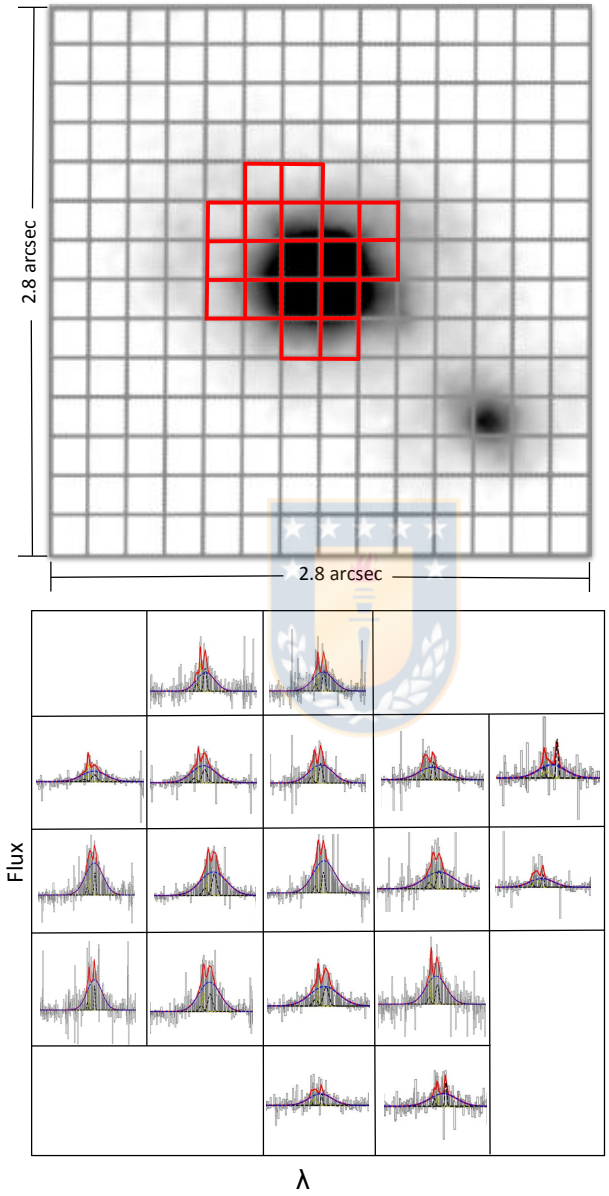

Figure 3.2.1: Top: HST F850LP image of galaxy ID=557 with the KMOS field of view split in its 14×14 spaxels (boxes in grey color). The spaxels marked in red correspond to the 18 spaxels with S/N > 5. Bottom: the best multi-gaussian fits for each spaxel showed in red boxes in the top panel.

The BLR has only recently been resolved through the implementation of high generation instruments such as GRAVITY at the VLT (Gravity Collaboration et al. 2020a;b). Consequently, in this work we cannot consider the broad emission lines to the construction of velocity and flux distribution maps, therefore, the kinematics analysis was performed only for AGN ID=557, which has detection of narrow emission lines.

The following procedure was adopted to construct the velocity and velocity dispersion maps:

- From the best fit, we measured the average central wavelength of all spaxels.
- We estimate the redshift for each emission line using the following equation:

$$z = \frac{\lambda_{mean} - \lambda_{rest}}{\lambda_{rest}} \tag{3.2.2}$$

  Where λ_{mean} correspond to the average observed wavelength of all spaxels for each line.

- Then, we correct the center wavelength and wavelength dispersion values of each spaxel by the redshift found with equation 3.2.2 for each line using the expressions:

$$\lambda_{corr} = \frac{\lambda_{spaxels}}{z + 1} \tag{3.2.3}$$

  and,

$$\sigma_{corr} = \frac{\sigma_{spaxel}}{z + 1} \times 2.3548 \tag{3.2.4}$$

- Next, we calculate the velocity for each spaxel using the Doppler Effect equation for the light described as:

$$V = \frac{\lambda_{corr} - \lambda_{rest}}{\lambda_{rest}} \times c, \tag{3.2.5}$$

  where c correspond to the speed of light.

- Finally, we estimated the velocity dispersion for each spaxel through:

$$\sigma_{\rm v} = \frac{\sigma_{\rm corr}}{\lambda_{\rm mean}} \times {\rm c}. \tag{3.2.6}$$

Also, we corrected the FWHM for instrumental resolution $\mathrm{FWHM_{ins}}$ by setting $\mathrm{FWHM_{intrinsic}} = \sqrt{\mathrm{FWHM^2_{obs}} - \mathrm{FWHM^2_{ins}}}$ where $\mathrm{FWHM_{ins}}$ was obtained from the FWHM of sky lines.

Finally, the velocity maps and velocity dispersion maps constructed for AGN ID=557 are shown in figure 3.2.2 where, for visualization purposes, each KMOS spatial pixel has been simply interpolated using a 5x5 box.

Once the velocity maps are obtained, we measure the kinematic position angle (PA_{kin}) to know the direction and orientation of the gas movement using the method described by Rodrigues et al. (2016). For this, we first look for the maximum and minimum of velocity values in each map, where we define as peaks the values that are ∼2 times greater than the average velocity. Then we define the PA_{kin} as the angle of the axis defined by the position of the maximum and minimum values. Such as is presented in table 3.2.1 and figure 3.2.3, we find more than one kinematical axis for the [NII] and Hα emission line.

On the other hand, using the velocity dispersion maps we also calculate the peaks in dispersion defined as the spaxels whose dispersion value is $\sim$ 1.5 times the average of the whole map.

As shown in tables 3.2.1 and 3.2.2, various velocity and velocity dispersion peak values have max/mean values below the limit defined according to the selection criteria, so they should not be considered as peaks. However, when performing a visual inspection of the maps and comparison with nearby spaxel values these effectively correspond to peaks.

Figure 3.2.4 presents the color image of galaxy ID=557 obtained from the F625W, F775W, and F850LP HST bands with the dispersion peaks positions denoted by red boxes. The kinematic axis measured for each detected emission line is shown in solid red lines. We observed that in all cases the velocity dispersion peaks are shifted concerning the photometric center of the galaxy measured in the analysis performed in section 3.3. Consequently, at first sight, this galaxy has perturbed kinematics according to the classification criteria proposed by Flores et al. (2006).

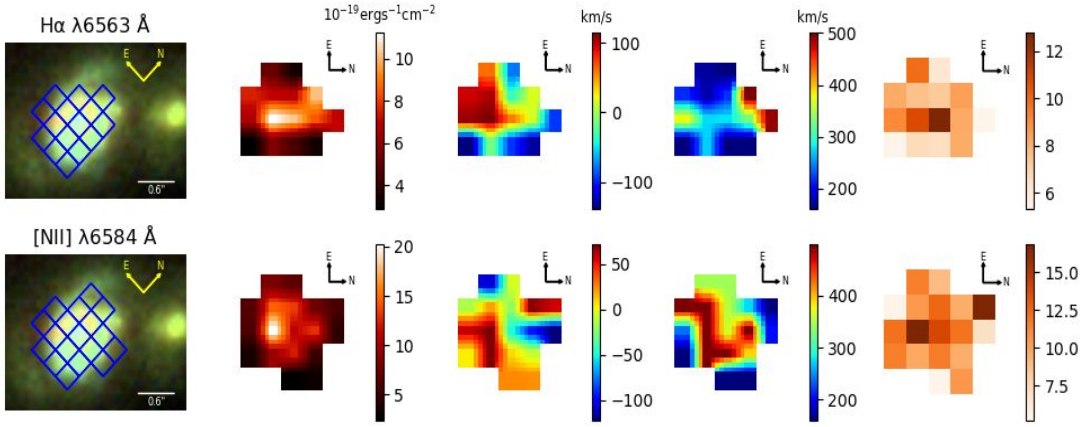

Figure 3.2.2: Kinematic characterization of AGN ID=557 in the cluster RXJ0152-137 at z=0.84 from the Hα and [NII] lines detected with KMOS instrument on the VLT. From left to right: the HST F850LP image and the spatial footprint covered by the KMOS spaxels with S/N>5 (blue boxes), flux distribution, the velocity fields, velocity dispersion maps, and the S/N maps for each detected emission feature. For visualization purposes, each spatial pixel in velocity and dispersion has been smoothed using a 5x5 box. At first view, this galaxy presents disturbed kinematics.

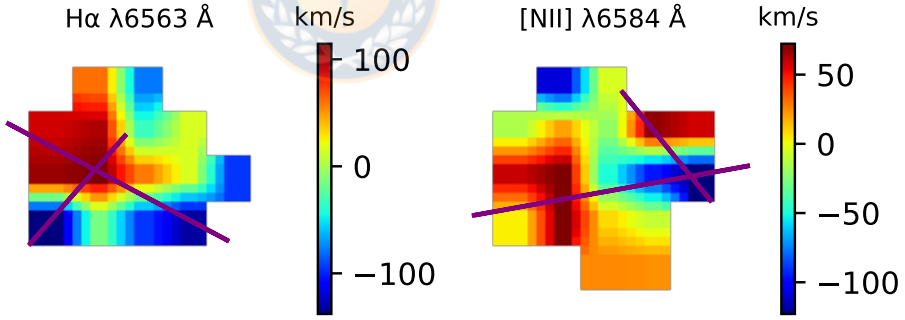

Figure 3.2.3: Velocity fields used to measure of PA$_{kin}$ by using the method described in Rodrigues et al. (2016). The purple lines in both maps show the kinematic axes found for each detected emission line in AGN ID=557. Both maps show two axes since there is more than one velocity peak on each map (see table 3.1.1).

Table 3.2.1: Velocity map parameters.

ID	Line	min [km s^{-1}]	min/mean	max [km s^{-1}]	max/mean	PA$_{kim}$[deg]
557	H$\alpha_{\rm narrow}$	-130	1.71	114	1.50	63
		-137	1.80	115	1.51	135
	[NII]	-122	2.65	72	1.56	99
		-122	2.65	69	1.50	44

Table 3.2.2: Velocity dispersion map parameters.

ID	Line	max [km s^{-1}]	max/mean
557	H$\alpha_{\rm narrow}$	501	1.90
		493	1.87
	[NII]	499	1.46
		499	1.46
		499	1.46
		499	1.46
		499	1.46

3.3 Photometric analysis

We performed a photometric analysis for both AGN using the HTS ACS/WFC imaging data in the broad band filter F850LP. The details of observation and data reduction are explained in Blakeslee et al. (2006). These data have also been used and described by Postman et al. (2005); Demarco et al. (2010) and Nantais et al. (2013).

We used the ELLIPSE IRAF task to fit elliptical isophotes on the images to characterize the surface brightness distribution. Within this task, there is the MAGPAR section, which controls the reference parameters to estimate and calibrate the source magnitude. Here the mag0 value (magnitude of the reference source taken as the instrumental magnitude of the zeropoint) was calculated through the following equation:

$$\mathrm{ZP_{ST}} = -2.5\log(\mathrm{PHOTFLAM}) - \mathrm{PHOTZPT}$$

where PHOTFLAM corresponds to the reverse sensitivity (in units of erg $\mathrm{cm^{-2}}$ $\mathrm{\AA^{-1}}$ $\mathrm{electron^{-1}}$), which represents the scale factor needed to transform an instrumental flux into units of electrons per second at a physical flux density, and PHOTZPT corresponds to the zero point of the STmag magnitude system whose value is -21.1. Both parameters are header keywords on the HST/ACS fits files.

To begin the fitting, we first mask and remove the neighboring galaxies from both AGN present in the images, to fit only the flux from the galaxies under study.

We carry out the fitting in INTERACTIVE mode to visualize in ds9, one by one, the isophotes fitted on the HST images and check that the fitting is consistent

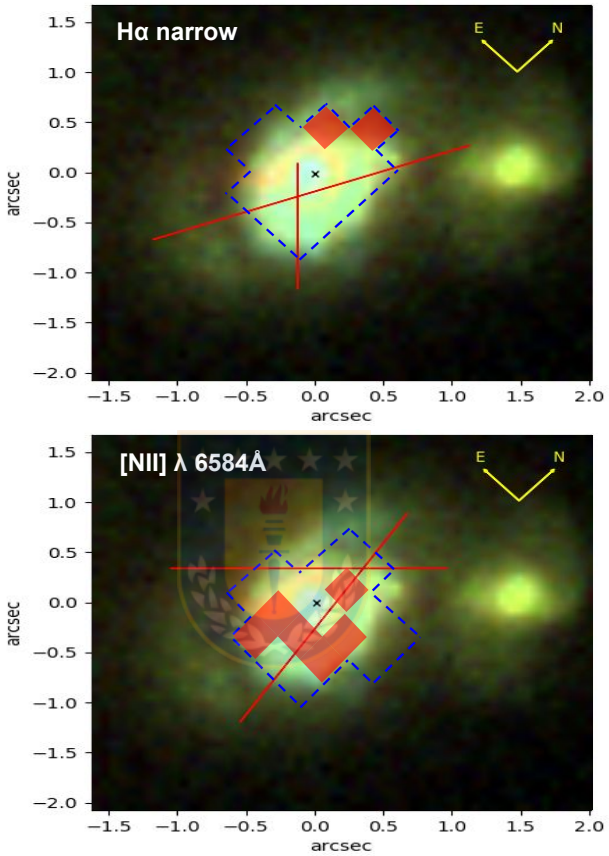

Figure 3.2.4: Measurement of the dispersion peak positions for the AGN ID=557. The figure shows the color image of the galaxy obtained with the HST in the F625W, F775W, and F850LP bands. The blue dashed contours show the detection area of each emission line. The kinematic axes found in each velocity map are shown by the solid red lines. In each image, the dispersion peaks are indicated with red squares of a size equivalent to the spaxel in which they were detected in. This AGN shows disturbing kinematics since it presents two kinematic axes and the dispersion peaks do not coincide with the photometric center of the galaxy (black cross) found in section 3.3.

Table 3.3.1: Parameters of the outermost fitted ellipse using the IRAF ELLIPSE task for each AGN.

ID	SMA [kpc]	ELLIP	PA [deg]	F850LP MAG
557	7.79	0.33 ± 0.01	60.41 ± 0.96	19.54 ± 0.01
300	7.08	0.44 ± 0.01	89.05 ± 1.58	19.64 ± 0.02

considering the most external isophote with 1σ above the background level the last one fitted to the data.

We considered the photometric position angle (PA_{phot}) as the PA for the outermost ellipse of the fitting whose parameters are shown in table 3.3.1. In figure 3.3.1 is shown the elliptical isophotes fitting to each galaxy with the PA_{phot} (solid red line).

3.4 Morphological analysis

3.4.1 Bar detection

It is well known that bars drive the secular evolution of galaxies, that is, a relatively slow evolution resulting from the movement of material through the bar. The bars are efficient in conducting the gas towards the center of the galaxy (see Sakamoto et al. 1999). This is due to a loss of angular momentum as bars are known to be efficient at transferring angular momentum from the center out. This can also change the orbits of the stars, thus giving a bars possible role in the formation of the bulge.

The non-symmetric potential of a bar can apply torques that result in a radial input of gas towards the galactic center, which produces high central concentrations of molecular gas and star formation in the nucleus. Once the gas is accumulated within the central ∼100 pc, additional dynamic instabilities could transport the gas in and feed the BH (Shlosman et al. 1989).

The possible connection between the existence of a bar and the activity of an AGN has been a matter of discussion in recent years. Cisternas et al. (2015) performed a comparison between the fraction of bars present in AGN and in inactive galaxies between $0.15 < z < 0.84$ using high-resolution HST images to identify the bars with the ELLIPSE/IRAF isophote fitting method. They found that the barred

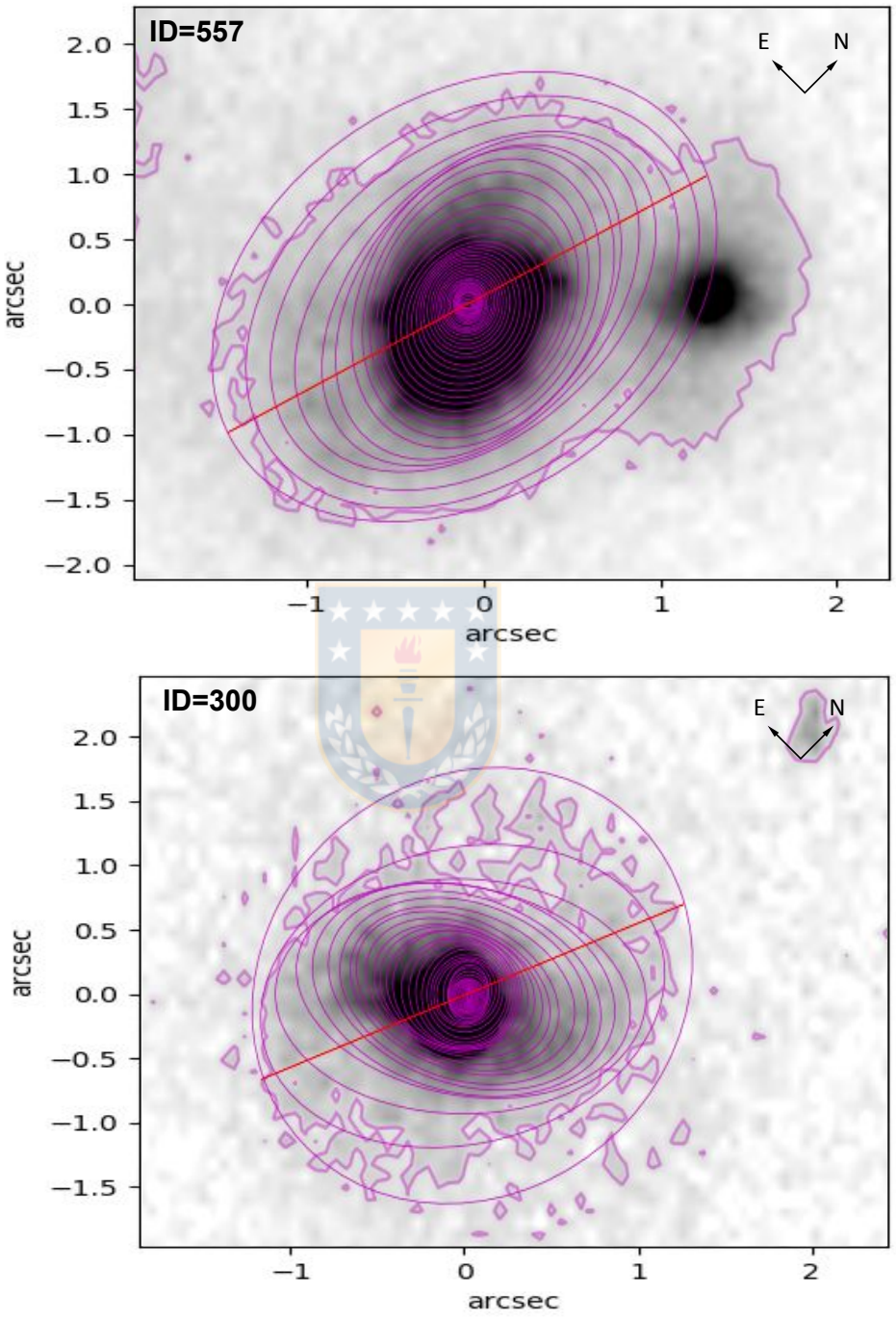

Figure 3.3.1: Fitting of the elliptical isophotes from the photometric analysis performed using the IRAF ELLIPSE task on the HTS ACS/WFC images in the F850LP band. The figure shows the best fitted isophotes in pink color, and the PA_{phot} obtained from the outermost ellipse in red, whose values are 60.41° ± 0.96 for ID=557 and 89.05° ± 1.58 for ID=300.

galaxy fraction decreases with redshift from 71%±10% at z ∼0.3 to 35%±7% at z ∼0.8, and also that the AGN strength is not influenced by the presence of a bar since both barred and unbarred galaxies show equivalent L_X brightness values within the redshift range studied. This suggest that the efficiency of AGN activity is independent of the large-scale structures of a galaxy.

On the other hand, studies at lower redshift show a possible connection of the effects of a bar on central star formation and between AGN activity, but with an analysis that turns out to be complex since this conclusion varies with sample properties such as color, morphology and stellar mass (Oh et al. 2011).

On the other hand, the analysis of the radial distribution of isophotes and their fitted parameters allows us to distinguish the presence of morphological structures such as bars, spiral arms, etc. The structure of a bar, for example, can be recognized by the variations of the values of ellipticity and PA. It is expected to find an increase in ellipticity until it reaches a maximum value (greater than 0.25) and then begins to decline by at least 0.1, while the PA values remain constant (within 10°), and then change at the transition point between the bar and the disk (Sheth et al. 2003; Marinova and Jogee 2007; Barazza et al. 2008). This analysis is based on the fact that the ellipses are expected to align with the PA of the bar and increase their ellipticity until the end of the bar. This is because in galaxies the bars appear as linear elliptical structures centered in the galaxy.

In the case of the presence of spiral arms, the variations of these parameters are more complex where the ellipticity can oscillate and the PA can change value abruptly (Barazza et al. 2008).

Figures 3.4.1 and 3.4.2 show the radial variation of the fitted parameters in the photometric isophotes analyses for each AGN. We observe that for galaxy ID=557, the ellipticity of the isophotes increases until reaching a maximum value of 0.374 and then has a slight drop of only ∼ 0.04. On the other hand, it is evident that the PA values do not remain constant but show a slight oscillation in the innermost part of the galaxy and then increase towards the outermost part, so this galaxy does not comply with any of the criteria described for the evident presence of a bar.

Moreover, for galaxy ID=300 we observe in figure 3.4.2 that, starting from a radius of $\sim$ 1.82 kpc outward, the ellipticity begins to increase until it reaches a maximum value of 0.45 and then decreases to values of $\sim$ 0.35. Also, in the same interval, the PA remains constant. With these two results, it is evident the presence of an internal structure in the form of a bar observable from $\sim$ 1.82 kpc to 7 kpc due to the PSF of the images, which corresponds to a value of 2 pixels (Nantais et al. 2013).

Finally, due to the non-detection of narrow lines in this galaxy, we cannot perform a spatial analysis of the kinematics, therefore it is not possible to directly analyze the connection between the bar and the internal kinematics of AGN ID=300.

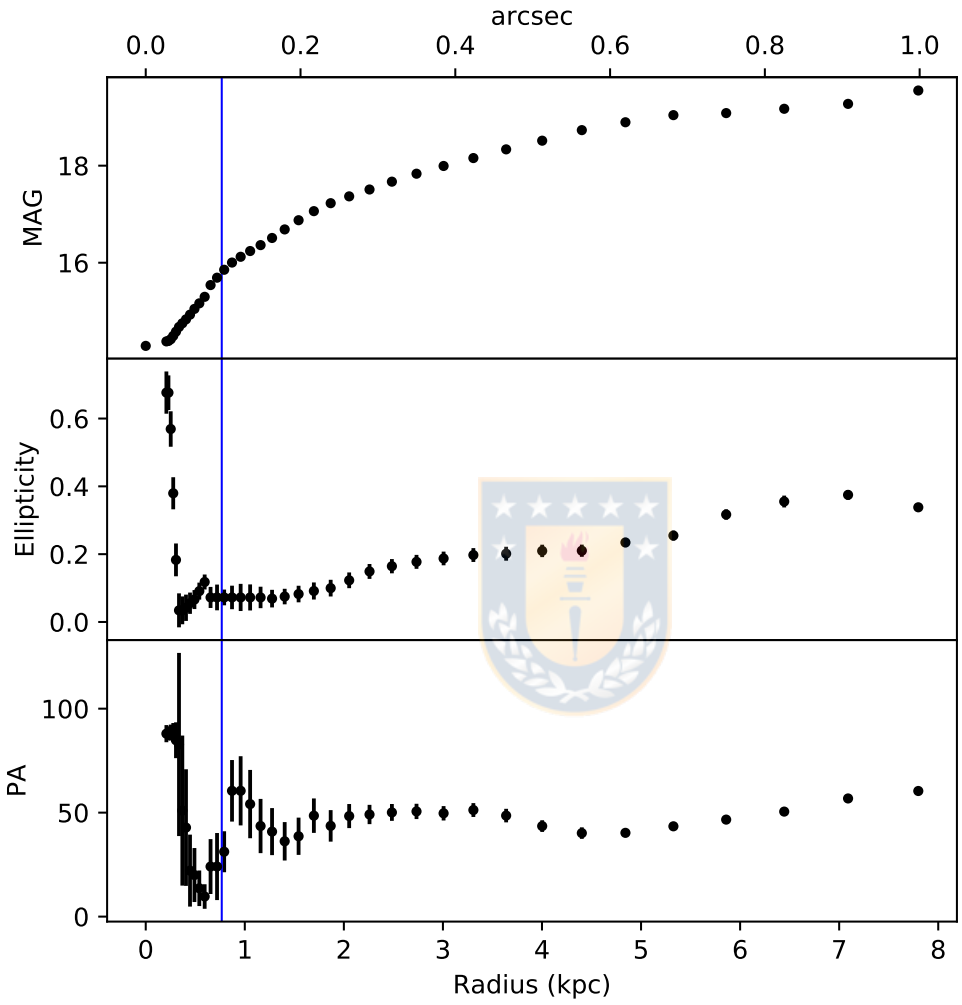

Figure 3.4.1: Radial variation of the measured parameters from the fitting of elliptical isophotes with the IRAF ELLIPSE task for AGN ID=557. From top to bottom: the magnitude, ellipticity, and PA of each ellipse as a function of radius in kpc and arcsec (secondary x-axis). The blue solid line denotes the FWHM of the PSF in the F850LP band, which corresponds to a value of 2 pixels according to Nantais et al. (2013). We observe that the PA value does not remain constant while the ellipticity increases, so that the presence of a bar cannot be guaranteed according to the criterion used by Marinova and Jogee (2007).

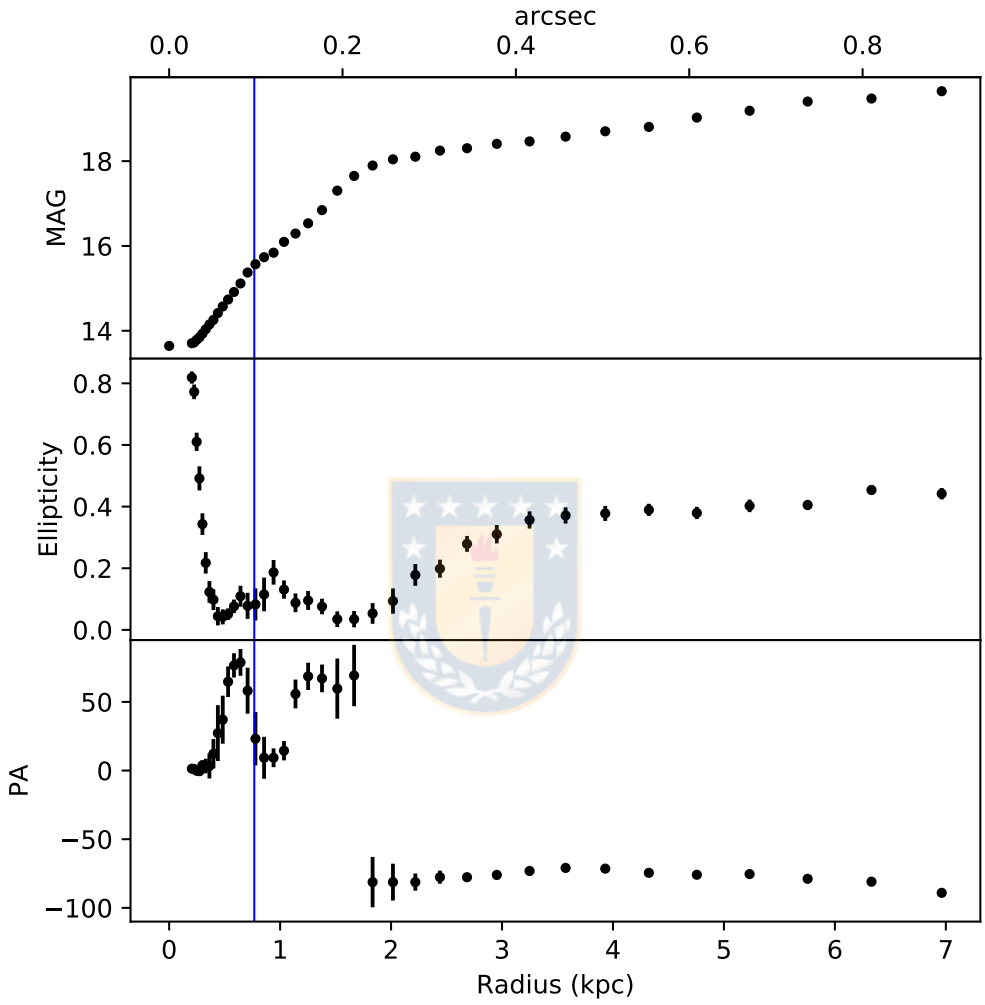

Figure 3.4.2: Radial variation of the measured parameters from the fitting of elliptical isophotes with the IRAF ELLIPSE task for AGN ID=300. From top to bottom: the magnitude, ellipticity, and PA of each ellipse as a function of radius in kpc and arcsec (secondary x-axis). The blue solid line denotes the FWHM of the PSF in the F850LP band, which corresponds to a value of 2 pixels according to Nantais et al. (2013). We observe that from a radius of ∼1.82 kpc there is evidence of the presence of a bar since the ellipticity gradually increases to a value of 0.45 and the PA remains constant.

3.4.2 Mopho-kinematic classification

The technique of IRAF ELLIPSE isophotes analysis is not sufficient to classify these galaxies morphologically. However, Nantais et al. (2013) shows the morphological analysis of 124 spectroscopically confirmed members of the cluster RXJ0152-1357 among which our sources are. In that work, for the morphological classification, they included color information, visual morphology, and a light profile fitting of galaxies with 1 or 2 components using the software GALFIT (Peng et al. 2002) on *riz* HST images following the classification criteria described by Neichel et al. (2008) and Delgado-Serrano et al. (2010). This analysis gave a Pec/M classification for the AGN ID=557 due to the blueness of its center and the possible interaction with its neighbor on the northwest that is clearly seen in the photometric images (see figure 3.2.4). On the other hand, a Pec/AGN classification was given to AGN ID=300, also because its center is considerably bluer than the rest of the galaxy which excluded it from the regular galaxy classification.

Rodrigues et al. (2016) carried out a morphological analysis very similar to that described by Nantais et al. (2013) in order to obtain a morpho-kinematic classification of AGN ID=557. Therefore, complementing our kinematic analysis and the morphological information, AGN ID=557 can be classified as Pec/CK, that is, peculiar morphology with a complex kinematics with two kinematic axes.

3.5 Emission line ratio

The most usual way to study the physical conditions of the NLR of an AGN is through the flux distribution of its emission lines. Especially, the flux ratio between its lines allows us to have an idea of the gas excitation level (ionization parameter) and its metallicity.

Figure 3.5.1 shows the integrated flux distribution maps for each line detected in AGN ID=557. The emission peak is shown in blue squares whose size indicates the size of the spaxel where the line was detected. The peaks of the narrow $H\alpha_{narrow}$ and [NII] lines are detected within the same spaxel shifted $0.2''$ to the photometric center of the galaxy, equivalent to a distance of $\sim$1.56 kpc for a z=0.8672. The fact that both lines have their higher emission in the same spaxel supports the assumption made in section 3.1 for the fitting of the lines that they originate in

the same gas cloud.

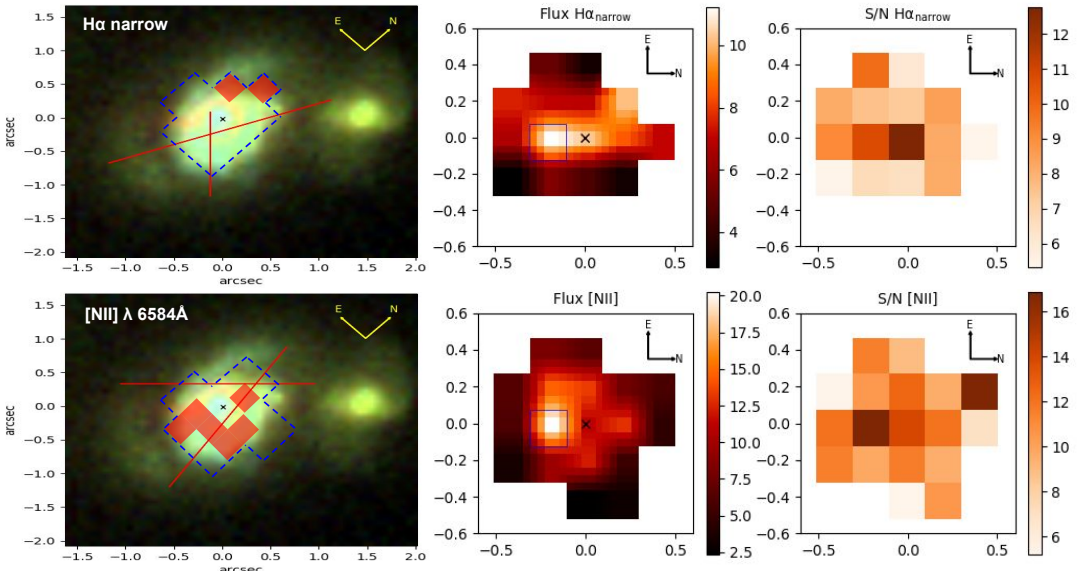

Figure 3.5.1: Left: Kinematics information described in figure 3.2.4. Right: Integrated flux maps of emission lines detected in AGN ID=557 and S/N maps. The black cross indicates the photometric center of the galaxy found in section 3.3. The blue squares indicate the position of the spaxel where the emission peaks of each line were detected. The peaks for Hα_{narrow} and [NII] emission come from the same spaxel whose center is offset by 0.2″ from the photometric center, equivalent to ∼1.56 kpc of distance at z = 0.8672. For visualization purposes, each original KMOS spaxel has been linearly interpolated into 5x5 squares on the flux maps.

On the other hand, diagnostic diagrams such as BPT (Baldwin et al. 1981) allow separating HII regions of star formation from AGN activity areas depending on the values of the [NII]/Hα and [OIII]/Hβ flux ratios, all of which correspond to tracer lines of ionized gas from the NLR that, depending on its abundance, will determine the process behind its ionization. With integral field spectroscopy, we can produce maps of these ratios and observe their distribution spatially, thus allowing us to visualize the ionizing power range of the AGN and to differentiate within a galaxy between the zones of action of the BH and star formation.

According to the lines described by Kewley et al. (2001a) and Kauffmann et al. (2003) the values of log([NII]/Hα) from -0.2 to 0.2 are the results of a gas ionization due to a combination between AGN and star formation, while for values higher than 0.2 it corresponds to only AGN or LINERs.

The ratio [NII]/Hα is an indicator of metallicities because the [NII] corresponds to a secondary element, where the metallicity of the galaxy increases as the value

of the ratio increases, i.e. in the presence of more [NII].

Figure 3.5.2 shows the distribution map of log([NII]/Hα_{narrow}) for AGN ID=557. Note that the maximum value of the ratio is offset from the photometric center. Also, areas with values greater than 0.2 are distributed in two peaks, one towards the East and the other towards the North-East of the galaxy. On the other hand, we do observe values of [NII]/Hα_{narrow} that may be associated with star formation. However, since we do not know the value of another flux ratio such as [OIII]/Hβ in those regions, we cannot distinguish whether it corresponds to HII regions of star formation or only a zone of the very low metallicity of a pure AGN.

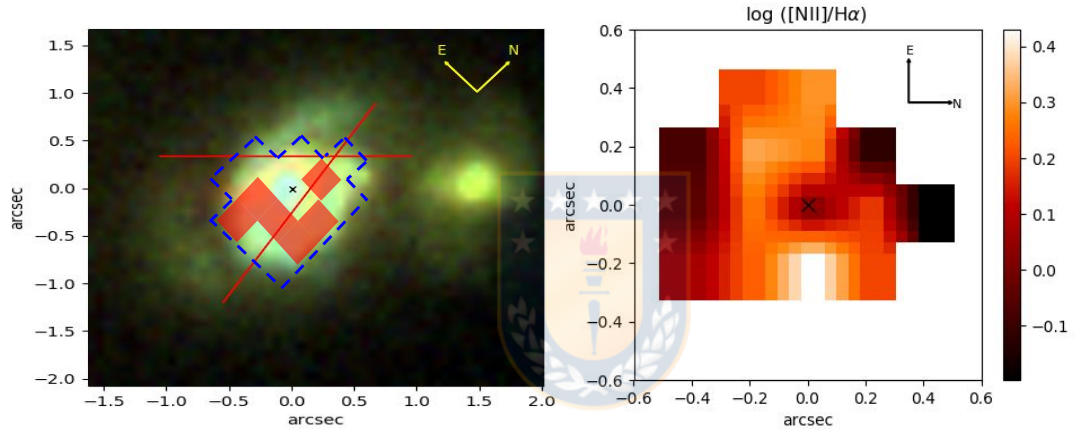

Figure 3.5.2: Left: Color image of AGN ID=557. The blue segmented line shows the contour of log([NII]/Hα) distribution map with the kinematic information of the [NII] emission line as described in figure 3.2.4. Right: log ([NII]/Hα) distribution maps. Visually, it is evident that the highest log([NII]/Hα) values do not coincide with the photometric center (black cross). Also, zones with values greater than 0.2 are distributed in two peaks, one towards the East and the other one towards the Northeast of the galaxy. The distribution of emission associated with AGN activity has a morphology similar to that of areas of high velocity dispersion for [NII] (red squares), which may be associated with the presence of radial outflows.

To distinguish globally if the galaxy ID=557 corresponds to a combination between star formation and AGN, or only to pure AGN we look for the integrated values of the ratios [NII]/Hα from the KMOS data and [OIII]/Hβ using the data from the FORS2 instrument on the VLT provided by Demarco et al. (2005).

Similar to that described in section 3.1 for Hα and [NII], we performed a multi-Gaussian fitting for the Hβ line and the doublet of [OIII]λ4959 Å and [OIII]λ5007 Å, using the Python LMFIT package. Figure 3.5.3 shows the integrated spectrum of the galaxy ID=557 in the rest frame together with the best fit to the profile of the emission lines (red line) and their respective Gaussian components (black dashed lines). Similar to that found for the profile of Hα, the presence of a broad component was detected for Hβ redshifted with respect to the narrow component at a velocity of 1,366 $\pm$ 166 km s^{-1} and a FWHM = 3,741 $\pm$ 339 km s^{-1}. On the other hand, for the lines of [OIII], the best fit involves the presence of two components for each line, a narrow one for the center line and a broad one for the base blueshifted to the center line at a velocity of $\sim$ -254 km s^{-1} and $\sim$ -252 km s^{-1} for [OIII]λ4959 Å, and [OIII]λ5007 Å, respectively. This blueshifted base, also called "blue wing", is associated with AGN outflows (Crenshaw et al. 2009). Table 3.5.1 shows the parameters for each emission line.

The log([OIII]/Hβ) flux ratio provides us with a value of 1.03, which, together with the log([NII]/Hα) = 0.11 value found from the KMOS data, locate the galaxy ID=557 within the pure AGN zone in the BPT diagram.

The emission of the broad basal component is expected to be higher for [OIII]λ5007 Å. However, the opposite is observed in the spectrum due to a loss of flux on the wavelength side of the line, which is generated by telluric absorption. This line corresond to the H_2O absorption line package with a spectral range of 4,964Å - 5,093Å (Rudolf, N. et al. 2016). Therefore, the correct detection of the broad component and the proper flux corresponding to the narrow component cannot be assured, so the location of this galaxy in the BPT diagram may vary vertically on the [OIII]/Hβ axis from the value 1.03 to lower values.

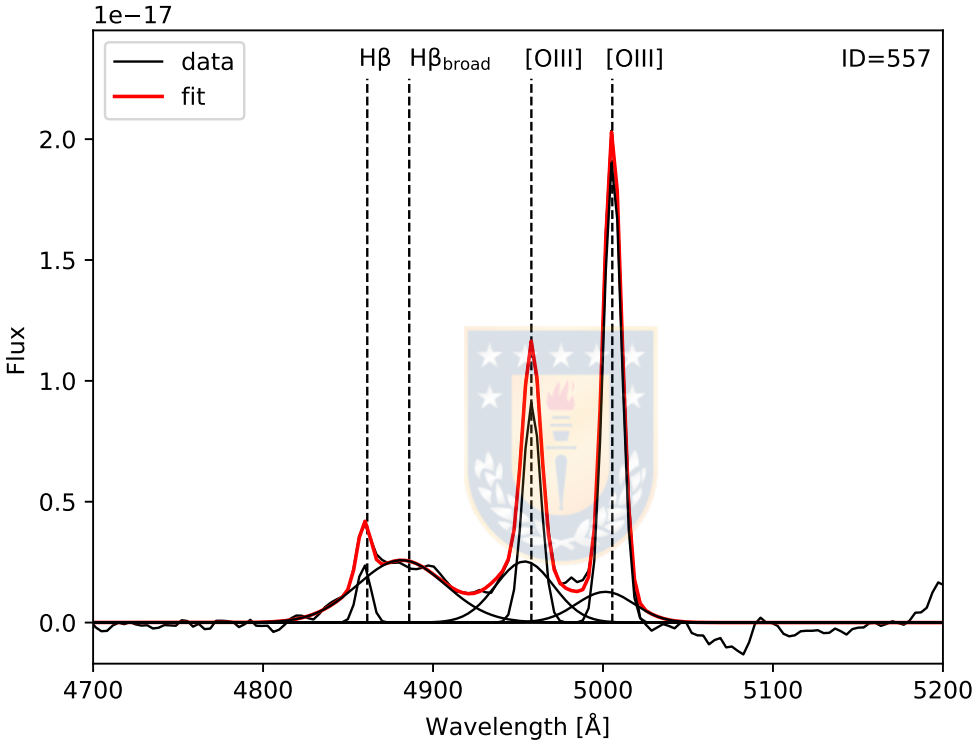

Figure 3.5.3: Integrated optical spectrum of galaxy ID=557 in rest-frame wavelength using data from the FORS2 instrument (Demarco et al. 2005). Figure shows the best fit to the profile of the Hβ lines and the [OIII] doublet (red curve), together with their respective Gaussian components (black curves) obtained by using Python LMFIT. Similar to that found in the section 3.1 for Hα, a redshifted broad component was detected for Hβ while for [OIII] the best fit considers a blue broad component for the base of each line ("blue wing") which is associated with AGN outflows (Crenshaw et al. 2009).

Table 3.5.1: Emission Line parameters of AGN ID=557's integrated spectrum from FORS2 (Demarco et al. 2005).

Line	λ_{obs} [Å]	FWHM $[kms^{-1}]$	Relative FLUX $[10^{-17}ergs^{-1}cm^{-2}]$
$H\beta_{narrow}$	4,859 ± 1	575 ± 149	0.70
$H\beta_{broad}$	4,881 ± 2	3,741 ± 339	4.95
$[OIII]_{blue}$	4,953 ± 2	2,424 ± 327	3.19
[OIII]	4,958 ± 1	760 ± 21	3.61
$[OIII]_{blue}$	5,001 ± 2	2,401 ± 324	1.60
[OIII]	5,005 ± 1	753 ±21	7.58

Chapter 4

Summary and Discussion

A summary of the principal results of each source is presented below.

4.0.1 AGN ID=557

This galaxy corresponds to a type 1 AGN, that is, it presents narrow lines from the NLR and broad lines from the BLR in the spectra obtained with KMOS and those presented by Demarco et al. (2005) using the FORS2 instrument. In both integrated spectra a redshifted broad component from low ionization Balmer emission lines is detected as Hα with a FWHM = 4,572 $\pm$ 179 km s^{-1} and a narrow line velocity of 938 $\pm$ 74 km s^{-1}, and Hβ with FWHM=3,741 $\pm$ 339 km s^{-1} and v = 1,366 $\pm$ 166 km s^{-1}. Zhang et al. (2009) identified this same feature in a sample of AGN at redshift z $<$ 0.37 from the SDSS DR4 (Adelman-McCarthy et al. 2006), suggesting that these objects correspond to a subclass of AGN called dbp-emitters (AGN with double-peak emission from Balmer lines) where part of the BLR emission, commonly the blue component, is obscured by dust due to characteristics such as the inclination of the galaxy.

On the other hand, this galaxy presents disturbed kinematics. This can be observed visually in the maps shown in figure 3.2.2 and through the analysis of the dispersion peaks and kinematic axes shown in figure 3.2.4, where it was found that the velocity map for each emission line presents two kinematic axes that are not coincident with the photometric axis. Also, both maps have at least two peaks in velocity dispersion which are shifted to the photometric center of the galaxy.

Also, from the photometric analysis performed in section 3.3 it can be seen that there is no presence of sub-structures such as a bar that may trigger the movement of material towards the center of the galaxy to feed the BH. On the other hand, this technique of isophotal fitting analysis with ELLIPSE from IRAF is not sufficient to perform a complete study of the morphology of the galaxy. Then, it is necessary to complement this analysis with other studies. Nantais et al. (2013) employing a light profile fitting technique using GALFIT, proposed a morphological classification for this galaxy of Pec/M, that is, a perturbed morphology with a possible merger, due to the blueness of its center compared to the rest of the galaxy and to a possible interaction with the nearby galaxy observed in its photometric images.

Complementing our kinematic analysis with the morphological classification of Nantais et al. (2013) we can obtain a morpho-kinematic classification, similar to that obtained for disk galaxies by Rodrigues et al. (2016). The classification for the AGN ID=557 is Pec/CK, that is, a peculiar morphology with complex kinematics with two kinematic axes. This indicates that it is a non-virialized system where a strong mismatch is observed between the distribution of the stars and the ionized gas, mainly attributable to the activity of the AGN.

Analyzing the flux distribution and the [NII]/Hα flux ratio maps we observe that the peak emission for the broad component of Hα coincides with the center of the galaxy. However, the maximum value of [NII]/Hα is not centered as normally expected for an AGN. The map shows two peaks running relative to the photometric center, towards the East and Northeast of the galaxy, as shown in figure 3.5.2. The emission distribution associated with AGN activity presents a morphology similar to the high velocity dispersion zones for [NII] which can be associated with the presence of radial outflows. Besides, the map of [NII]/Hα shows some values lower than 0.2, related, according to the BPT diagram (Baldwin et al. 1981), to a composition of star-forming and AGN. To distinguish globally whether or not this galaxy has HII regions of star formation, we complement the value of integral [NII]/Hα with the value of [OIII]/Hβ measured from the optical spectrum of FORS2 provided by Demarco et al. (2005). A multi-Gaussian fit to the emission line profile detected the presence of a narrow and a broad component for Hβ, while for the [OIII] doublet the line profile indicates the presence of a central narrow component and a blue broad base known as "blue wing" associated

with the presence of biconical outflows (see Crenshaw et al. 2009). However, due to the contamination produced by telluric absorption, there was a loss of flux in the red part of the line [OIII]λ5007, so the broad component of it is not correctly detected. The lack of this information causes the flux measurement of the line to be unreliable so the ratio values for [OIII]/Hβ may decrease from the value equal to 1.03. However, because the value of [NII]/Hα = 0.11, this galaxy is positioned in the AGN pure zone of the BPT diagram.

4.0.2 AGN ID=300

This galaxy also corresponds to a type 1 AGN. However, the emission from the NLR is not observable in the spectral range of the KMOS YJ band since the narrow lines of Hα and [NII] are not distinguishable. The spectrum of this AGN only shows the broad component of Hα with a FWHM = 3,865 $\pm$ 101 km s^{-1}. This is also observed in low redshift AGN where, for example, Torres-Papaqui et al. (2020) found that in a sample of 3,896 Seyfert 1 (Sy1) galaxies at z$<$ 0.4, 36% of galaxies present only broad emission lines (called Sy1B). They also found differences with the Sy1 which do show narrow components (called Sy1N) reporting that the velocity of outflows are higher in the Sy1B than in the Sy1N which suggest different physical conditions in the Inter Stellar Medium, in particular, that the Sy1N have more gas in their NLRs than the Sy1B.

For this galaxy, it is not possible to perform a spatial analysis since we only observer the unresolved BLR.

On the other hand, from the isophotes analysis presented in section 3.3, it is possible to infer the presence of a bar structure which could be related to the activity of the AGN, where the asymmetric potential of the bar drives the movement of the gas towards the center of the galaxy feeding the BH (Sakamoto et al. 1999; Shlosman et al. 1989). However, there is no clear evidence of the influence of the bar on the internal kinematics because we cannot spatially resolve the kinematics of this AGN.

Similar to that found for AGN ID=557, Nantais et al. (2013) classified the AGN ID=300 morphologically as a Pec/AGN, that is, an AGN with a peculiar morphology due to the blueness of his center.

Furthermore, for AGN ID=300, as observed in the section 3.1, the narrow Hα and [NII] emission lines were not detected. The lack of the latter line is possibly an indicator of the low metallicity of the galaxy. This is consistent with the characteristics of the spectra obtained by Demarco et al. (2005), where for this galaxy no significant emission was found from [OII] and [OIII] lines.

4.0.3 Discussion

It is known that AGN, due to their time evolution and metal production, show super-solar metallicities (Z > 2Z$\odot$; Nagao, T. et al. 2006; Matsuoka, K. et al. 2009), so low-metallicity AGN are very rare. Groves et al. (2006) conducted a low-metallicity AGN analysis on a a sample of ∼23,000 Seyfert 2 galaxies at an average redshift of 0.1 in the SDSS DR4. They used criteria to select low mass galaxies under the assumption of a correlation of mass and metallicity with the [NII]/Hα flux ratio. A classical example of such correlation in the local universe can be found, e.g., in (Tremonti et al. 2004). They showed that the low-metallicity AGN are characterized by a high value of [OIII]/Hβ and a very low value of [NII]/Hα for the photoionization model. From that sample, only ∼40 galaxies correspond to AGN candidates with metallicities lower than solar which indicates the infrequency with which this type of galaxies is found at low redshift. From this, a good way to detect low-metallicity AGN is through emission line diagnostics involving the [NII]/Hα flux ratio because the relative abundance of nitrogen is proportional to the metallicity due to its nature as a secondary element (van Zee et al. 1998). Thus, given the values of [OIII]/Hβ and [NII]/Hα, these AGN are generally found between the sequence of star-forming galaxies and AGN, a region of the BTP diagram known as "BPT Valley" where galaxies with high electron density and high ionization parameter are also located (see Kawasaki et al. 2017).

Therefore, according to the flux ratio values, a metallicity of ∼4Z$_\odot$ can be estimated for AGN ID=557, based on its location in the BTP diagram of Fig.2, shown in (Groves et al. 2006). This indicates that this AGN is an example of high metallicity AGN. Moreover, although we cannot have an estimate of the metallicity of the galaxy due to the non-detection of [NII], it is possible to infer that it is a low-metallicity AGN. Therefore, this AGN may be an example of a low-metallicity AGN at high redshift (z = 0.8201).

4.0.3.1 Environmental influence

Although both galaxies correspond to the same AGN type and show similar morphological characteristics, we have found a significant difference in the emission lines, where the detection or not of the [NII] emission line and no significant emission was found for [OII] and [OIII] lines in AGN=300, may be an indicator of the difference in metallicities between both AGN. Is it possible that this difference is related to the environment where these galaxies are located? As already mentioned, both galaxies are confirmed members of the cluster of galaxies RX J0152.7-1357 at z=0.84. However, they are located in different regions of the cluster. AGN ID=557 is located in the central part where there is a higher density of galaxies (Demarco et al. 2005; 2010; Jørgensen et al. 2005), gas (Maughan et al. 2003; Demarco et al. 2005; 2010) and dark matter (Jee et al. 2005). Also, this zone corresponds to the area that divides the two main substructures of the cluster (Demarco et al. 2005; Girardi et al. 2005), whereas AGN ID=300 is located in a more outer region where the density of the cluster components decreases considerably, as shown in the figure 4.0.1.

Studies have shown that AGN are less frequent in galaxy cluster environments than in low-density areas such as the field (Dressler et al. 1985; Ehlert et al. 2014), and a clear dependence on redshift is reported where the frequency of AGN in galaxy clusters increases with increasing redshift (Galametz et al. 2009; Pentericci et al. 2013; Martini et al. 2013; Bufanda et al. 2016). This is interpreted as evidence that the AGN population in clusters has evolved faster than the field population from at least z$\sim$1.5 to the present (see Martini et al. 2013).

There is convincing evidence that galaxy mergers and interactions play an important role in the triggering and evolution of AGN where the prevailing theoretical framework is that the most luminous AGN and starbursts are triggered by major mergers of gas-rich galaxies (Barnes and Hernquist 1991; Hopkins et al. 2006; 2008; Treister et al. 2010; 2012). In a cluster environment, additional mechanisms may interfere with the transport of cold gas that serves as the main fuel for the central black hole. These processes include the removal of the cold gas by the ram-pressure stripping process (Gunn and Gott 1972; Sheen et al. 2017), evaporation of the gas due to the high temperature in the ISM (Cowie and Songaila 1977), tidal effects due to the cluster potential (Farouki and Shapiro 1981; Merritt 1983; Gnedin 2003) and other galaxies (Richstone 1976; Moore

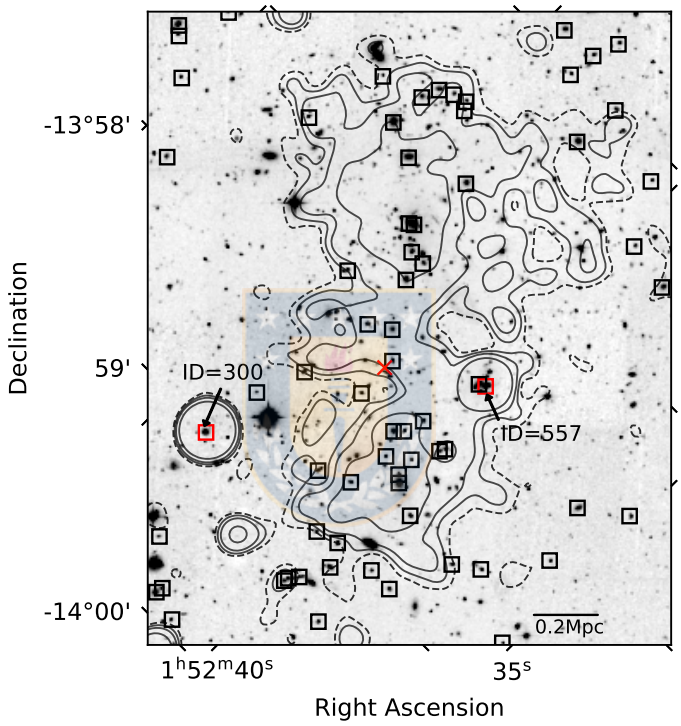

Figure 4.0.1: HST F850LP image of the central region of the galaxy cluster RX J0152.7-1357 at z=0.84. The figure shows the distribution of confirmed cluster members denoted by blue squares and the position of the two AGN in question concerning the cluster center (red cross) estimated by Girardi et al. (2005). The contours correspond to X-ray emission levels 5, 7, 10 and 20 σ above the background in the [0.5-2] keV band, FITS images provided by Demarco et al. (2005).

et al. 1996), and a lack of gas due to the absence of new cold gas infiltration (Larson et al. 1980). On the other hand, Poggianti et al. (2017) suggests that the mechanism of ram-pressure stripping may act as a trigger for the activity of an AGN by causing gas to flow towards the center of the galaxy. Therefore, the physical mechanisms that contribute to the triggering or suppression of the AGN activity are still a matter of debate, especially at high redshifts where the fraction of clusters decreases and the analysis of these processes in this type of environment becomes more complex.

Therefore, the difference in metallicities between these two AGN may be due to the region of the cluster where they are located and the physical processes associated with this type of environment to which they may have been exposed to.

In the case of AGN ID=557, which is in the innermost region near the cluster center, their high metallicity indicates that their host galaxy is in a major evolutionary stage where it has already consumed much of its gas for star formation and much of it has evolved to enrich its ISM, which can be observed through emission lines such as [NII]. On the other hand, considering a virial radius of the cluster of ∼1.4 Mpc (Maughan et al. 2003) and assuming that the galaxy falls at a speed of ∼250 km/s (Girardi et al. 2005), we note that this galaxy may have taken about ∼3 Gyr to reach its observed position. If we compare with the typical life time of an AGN ($\sim 10^5$ yr; Schawinski et al. 2015), it is evident that this galaxy suffered the activation of its BH during its fall to the cluster where some of the processes mentioned before could accelerate its star formation and also feed its central black hole.

Also, from the photometric images and some characteristics in the kinematic maps we can infer the possible interaction of AGN ID=557 with a neighboring galaxy when observing the surface brightness flux contours in the HST images (see figure 4.0.2). A common structure between ID=557 and the other galaxy present in the image can be seen which may correspond to a halo of stars ripped off from both galaxies by the tidal forces during the collision process. Also, it is visible the presence of other substructures associated with the possible interaction in the form of a cometary feature in the secondary galaxy that coincides with the position of one of the arms of ID=557. This seems to produce a bridge-like substructure, connecting (in projection) those objects, and whose position also coincides with the peaks in velocity dispersion for the Hα narrow component, as

shown in figure 4.0.2, thus indicating a possible excitation of the ionized gas in that zone product of the merger. It is known that interactions between galaxies can lead to a loss of angular momentum of the gas in the interstellar medium, bringing, as a consequence, material towards the galactic center (Barnes and Hernquist 1991). In this way, it is possible to associate the interaction of ID=557 with its nearby galaxy as one of the processes responsible for the activation of its central black hole. However, this interpretation needs more data to confirm that this other galaxy is a member of the cluster. In fact, not redshift for this secondary, possibly interacting galaxy has been previously reported in the literature (Jørgensen et al. 2005; Demarco et al. 2005; 2010).

On the other hand, for AGN ID=300 is easy to infer that this galaxy has probably not yet suffered the physical processes that could accelerate its star formation and therefore increase its metallicity as it happens to be most likely the case of AGN ID=557, due to the position in the cluster where they are observed. This can be interpreted as evidence of the effects of the environment on AGN and consequently on the evolution of galaxies where processes related to high density regions play an important role in accelerating star formation and triggering AGN activity. However, this study must be complemented with an integral field spectroscopy analysis of a larger sample of galaxies in the same region of the cluster, to study the environment around these AGN. Consequently, our future plan is to study a sample of galaxies from different galaxy clusters (including RXJ0152-137) and their field counterparts using higher-resolution instruments such as MUSE on the VLT. More concretely, we plan to combine the kinematics of galaxies in field and clusters with deep high-resolution images, multi-band photometry, and spectrometry to construct a new, more enhanced scenario of galaxy formation and evolution at high redshift.

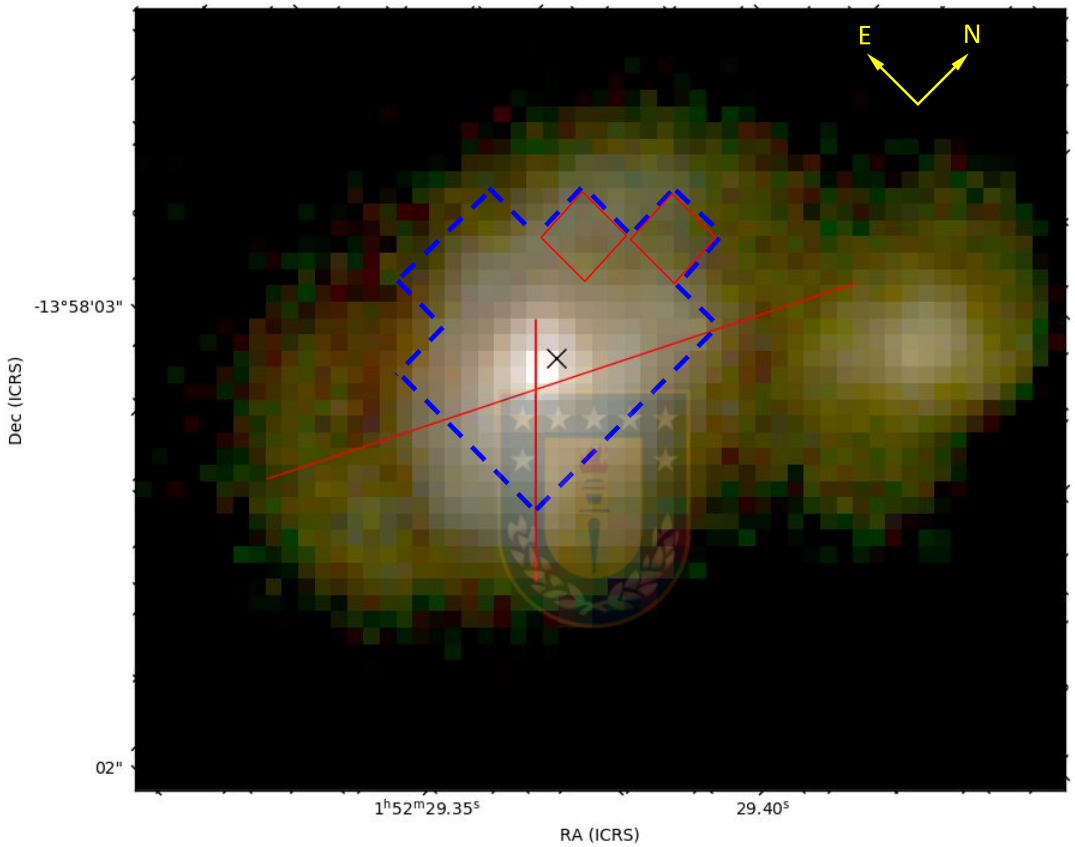

Figure 4.0.2: Color image of AGN ID=557. The blue dashed line indicates the region where the Hα narrow component was detected with the kinematic parameters described in figure 3.2.4 and shown here in red color. It is evident the presence of a common envelope of stellar material between the galaxies and a diffuse bridge-like substructure from one of the arms toward the nearby galaxy. Also, the velocity dispersion peaks (shown with red squares) coincide with the start of the bridge which could be evidence of possible galaxy interaction.

Chapter 5

Conclusion

The technique of integral field spectroscopy in the near-infrared with KMOS at the VLT allowed us to spatially resolve the kinematics of one AGN member of the cluster RX J0152.7-1357 at z=0.84. This was done by performing a multi-Gaussian fitting to the emission line profiles which enabled the subsequent construction of the velocity and velocity dispersion maps. By combining the kinematical analysis with the photometric analysis through HST images and previous information on this galaxy, we are able to obtain a more complete view of the properties of this AGN, and also, to compare it with other AGN of the same galaxy cluster to identify differences that may be related to the cluster environment in which they develop.

In summary, the main results of this investigation are:

- Both AGN have a rest-frame optical spectrum with characteristics of type 1 AGN.
- The integrated spectrum of AGN ID=557 presents a broad component redshifted with respect to the narrow component for Balmer emission lines. This could be evidence that this AGN corresponds to a type of AGN called dbp-emitters, which would be partially obscured by the torus according to Zhang et al. (2009).
- AGN ID=557 can be classified morpho-kinetically as Pec/CK, i.e, a galaxy with peculiar morphology with complex kinematics. The kinematic analysis shows the presence of more than one kinematic axis and several velocity

dispersion peaks which suggest that this galaxy corresponds to a non-virialized system. This indicates a possible previous event such as a merger or other interaction.

- For the AGN ID=557, the kinematics maps complemented with the log([NII]/Hα) distribution maps, show evidence of a radial outflow which is supported by the detection of the "blue wings" in the [OIII] emission line in the FORS2 spectrum.

- The values of log([NII]/Hα)=0.11 and log([OIII]/Hβ)=1.03 place the AGN ID=557 in the AGN-pure zone of the BPT diagram. However, the value of [OIII]/Hβ is not certain due to the loss of flux caused by telluric absorption in the FORS2 spectrum.

- Based on what it is proposed by Groves et al. (2006) about the relation between metallicity and the [NII] emission line strength, we can say that the AGN ID=557 corresponds to a high metallicity AGN with a value of $Z = \sim 4Z_{\odot}$, while the AGN ID=300 may correspond to an example of low metallicity AGN at high redshift due to the lack of [NII] emission and the non-significant detection of [OII] and [OIII] emission lines on the FORS2 spectrum.

- The difference between the inferred metallicities of each AGN may be related to their location in the galaxy cluster. The AGN ID=557 has probably undergone processes that accelerated its evolution, therefore enhancing its metallicity during its passage through the cluster. Also, we have observed tentative evidence of possible ongoing interaction of this AGN with a neighboring galaxy, which is suggested by the HST images and the position of the narrow Hα velocity dispersion peaks.

Bibliography

J. K. Adelman-McCarthy, M. A. Agüeros, S. S. Allam, K. S. J. Anderson, S. F. Anderson, J. Annis, and et al. *The Astrophysical Journal Supplement Series*, 162(1):38–48, Jan. 2006.

J. Aird, A. L. Coil, A. Georgakakis, K. Nandra, G. Barro, and P. G. Pérez-González. *Monthly Notices of the Royal Astronomical Society*, 451(2):1892–1927, Aug. 2015.

D. M. Alexander and R. C. Hickox. *Nature*, 56(4):93–121, June 2012.

R. Antonucci. *Annual Review Astronomy and Astrophysics*, 31:473–521, Jan. 1993.

Astropy Collaboration, T. P. Robitaille, E. J. Tollerud, P. Greenfield, M. Droettboom, E. Bray, T. Aldcroft, M. Davis, A. Ginsburg, A. M. Price-Whelan, W. E. Kerzendorf, A. Conley, N. Crighton, K. Barbary, D. Muna, and H. e. a. Ferguson. *Astronomy and Astrophysics*, 558:A33, Oct. 2013.

Astropy Collaboration, A. M. Price-Whelan, B. M. SipHocz, H. M. G"unther, P. L. Lim, S. M. Crawford, S. Conseil, D. L. Shupe, M. W. Craig, N. Dencheva, A. Ginsburg, and et al. *The Astronomical Journal*, 156(3):123, Sept. 2018.

E. Bañados, B. P. Venemans, C. Mazzucchelli, E. P. Farina, F. Walter, F. Wang, R. Decarli, D. Stern, X. Fan, F. B. Davies, J. F. Hennawi, R. A. Simcoe, M. L. Turner, H.-W. Rix, J. Yang, D. D. Kelson, G. C. Rudie, and J. M. Winters. *Nature*, 553(7689):473–476, Jan. 2018.

R. Bacon, M. Accardo, L. Adjali, H. Anwand, S. Bauer, I. Biswas, J. Blaizot, D. Boudon, S. Brau-Nogue, J. Brinchmann, and P. e. a. Caillier. The MUSE second-generation VLT instrument. volume 7735 of *Society of Photo-Optical Instrumentation Engineers (SPIE) Conference Series*, page 773508, July 2010.

J. A. Baldwin, M. M. Phillips, and R. Terlevich. *Publications of the Astronomical Society of the Pacific*, 93:5–19, 1981.

F. D. Barazza, S. Jogee, and I. Marinova. *The Astrophysical Journal*, 675:1194–1212, 2008.

J. E. Barnes and L. E. Hernquist. *Astrophysical Journal Letters*, 370:L65, 1991.

R. Bassett, C. Papovich, J. M. Lotz, E. F. Bell, S. L. Finkelstein, J. A. Newman, K.-V. Tran, O. Almaini, C. Lani, M. Cooper, D. Croton, A. Dekel, H. C. Ferguson, D. D. Kocevski, A. M. Koekemoer, D. C. Koo, E. J. McGrath, D. H. McIntosh, and R. Wechsler. *The Astrophysical Journal*, 770(1):58, June 2013.

V. Beckmann and C. R. Shrader. *Active Galactic Nuclei*. 2012.

J. P. Blakeslee, B. P. Holden, M. Franx, P. Rosati, R. J. Bouwens, R. Demarco, H. C. Ford, N. L. Homeier, G. D. Illingworth, M. J. Jee, S. Mei, F. Menanteau, G. R. Meurer, M. Postman, and K.-V. H. Tran. *The Astrophysical Journal*, 644 (1):30–53, June 2006.

E. Bufanda, D. Hollowood, T. E. Jeltema, E. S. Rykoff, E. Rozo, P. Martini, T. M. C. Abbott, F. B. Abdalla, S. Allam, M. Banerji, A. Benoit-Lévy, and et al. *Monthly Notices of the Royal Astronomical Society*, 465(3):2531–2539, 12 2016.

H. Butcher and J. Oemler, A. *The Astrophysical Journal*, 285:426–438, 1984.

M. Cisternas, K. Sheth, M. Salvato, J. H. Knapen, F. Civano, and P. Santini. *The Astrophysical Journal*, 802(2):137, 2015.

C. Collet, N. P. H. Nesvadba, C. De Breuck, M. D. Lehnert, P. Best, J. J. Bryant, R. Hunstead, D. Dicken, and H. Johnston. *Astronomy and Astrophysics*, 586: A152, Feb. 2016.

L. L. Cowie and A. Songaila. *Nature*, 266:501–503, 1977.

D. M. Crenshaw, H. R. Schmitt, S. B. Kraemer, R. F. Mushotzky, and J. P. Dunn. *The Astrophysical Journal*, 708:419–426, 2009.

R. I. Davies, A. Agudo Berbel, and E. Wiezorrek. *Astronomy and Astrophysics*, 558:A56, 2013.

R. L. Davies, N. M. Förster Schreiber, H. Übler, R. Genzel, D. Lutz, A. Renzini,

S. Tacchella, L. J. Tacconi, S. Belli, A. Burkert, C. M. Carollo, R. I. Davies, R. Herrera-Camus, S. J. Lilly, C. Mancini, T. Naab, E. J. Nelson, S. H. Price, T. T. Shimizu, A. Sternberg, E. Wisnioski, and S. Wuyts. *The Astrophysical Journal*, 873(2):122, Mar. 2019.

R. L. Davies, N. M. F. Schreiber, D. Lutz, R. Genzel, S. Belli, T. T. Shimizu, A. Contursi, R. I. Davies, R. Herrera-Camus, M. M. Lee, T. Naab, S. H. Price, A. Renzini, A. Schruba, A. Sternberg, L. J. Tacconi, H. Übler, E. Wisnioski, and S. Wuyts. *The Astrophysical Journal*, 894(1):28, May 2020.

R. Delgado-Serrano, F. Hammer, Y. B. Yang, M. Puech, H. Flores, and M. Rodrigues. *Astronomy and Astrophysics*, 509:A78, 2010.

R. Demarco, P. Rosati, C. Lidman, N. Homeier, E. Scannapieco, N. Benitez, V. Mainieri, M. Nonino, M. Girardi, A. Stanford, P. Tozzi, S. Borgani, J. Silk, G. Squires, and T. Broadhurst. *Astronomy and Astrophysics*, 432, 2005.

R. Demarco, R. Gobat, P. Rosati, C. Lidman, A. Rettura, M. Nonino, A. van der Wel, M. J. Jee, J. P. Blakeslee, H. C. Ford, and et al. *The Astrophysical Journal*, 725(1):1252–1276, Nov 2010.

M. A. Dopita, Scharwächter, Julia, Shastri, Prajval, Kewley, Lisa J., Davies, Rebecca, Sutherland, Ralph, Kharb, Preeti, Jose, Jessy, Hampton, Elise, Jin, Chichuan, Banfield, Julie, Basurah, Hassan, and Fischer, Sebastian. *Astronomy and Astrophysics*, 566:A41, 2014.

A. Dressler. *The Astrophysical Journal*, 236:351–365, 1980.

A. Dressler, I. B. Thompson, and S. A. Shectman. *The Astrophysical Journal*, 288:481–486, Jan. 1985.

S. Ehlert, A. v. der Linden, S. W. Allen, W. N. Brandt, Y. Q. Xue, B. Luo, A. Mantz, R. G. Morris, D. Applegate, and P. Kelly. *Monthly Notices of the Royal Astronomical Society*, 437(2):1942–1949, 2014.

E. Ellingson, H. Lin, H. K. C. Yee, and R. G. Carlberg. *The Astrophysical Journal*, 547(2):609–622, Feb. 2001.

Event Horizon Telescope Collaboration and et al. 875(1):L1, Apr. 2019.

A. Fabian. *Annual Review of Astronomy and Astrophysics*, 50(1):455–489, 2012.

R. Farouki and S. L. Shapiro. *The Astrophysical Journal*, 243:32–41, Jan. 1981.

H. Flores, F. Hammer, M. Puech, P. Amram, and C. Balkowski. *Astronomy and Astrophysics*, 455, 2006.

N. M. Förster Schreiber, R. Genzel, M. D. Lehnert, N. Bouché, A. Verma, D. K. Erb, A. E. Shapley, C. C. Steidel, R. Davies, D. Lutz, N. Nesvadba, L. J. Tacconi, F. Eisenhauer, R. Abuter, A. Gilbert, S. Gillessen, and A. Sternberg. *The Astrophysical Journal*, 645(2):1062–1075, July 2006.

N. M. Förster Schreiber, R. Genzel, N. Bouché, G. Cresci, R. Davies, P. Buschkamp, K. Shapiro, L. J. Tacconi, E. K. S. Hicks, S. Genel, A. E. Shapley, D. K. Erb, C. C. Steidel, D. Lutz, F. Eisenhauer, S. Gillessen, A. Sternberg, A. Renzini, A. Cimatti, E. Daddi, J. Kurk, S. Lilly, X. Kong, M. D. Lehnert, N. Nesvadba, A. Verma, H. McCracken, N. Arimoto, M. Mignoli, and M. Onodera. *The Astrophysical Journal*, 706(2):1364–1428, Dec. 2009.

N. M. Förster Schreiber, A. Renzini, C. Mancini, R. Genzel, N. Bouché, G. Cresci, E. K. S. Hicks, S. J. Lilly, Y. Peng, A. Burkert, C. M. Carollo, A. Cimatti, E. Daddi, R. I. Davies, S. Genel, J. D. Kurk, P. Lang, D. Lutz, V. Mainieri, H. J. McCracken, M. Mignoli, T. Naab, P. Oesch, L. Pozzetti, M. Scodeggio, K. Shapiro Griffin, A. E. Shapley, A. Sternberg, S. Tacchella, L. J. Tacconi, S. Wuyts, and G. Zamorani. *The Astrophysical Journal Series*, 238(2):21, Oct. 2018.

A. Franceschini, G. Hasinger, T. Miyaji, and D. Malquori. *Monthly Notices of the Royal Astronomical Society*, 310(1):L5–L9, Nov. 1999.

A. Galametz, D. Stern, P. R. M. Eisenhardt, M. Brodwin, M. J. I. Brown, A. Dey, A. H. Gonzalez, B. T. Jannuzi, L. A. Moustakas, and S. A. Stanford. *The Astrophysical Journal*, 694(2):1309–1316, Apr. 2009.

R. Genzel, L. J. Tacconi, F. Eisenhauer, N. M. Förster Schreiber, A. Cimatti, E. Daddi, N. Bouché, R. Davies, M. D. Lehnert, D. Lutz, and et al. *Nature*, 442(7104):786–789, Aug 2006.

M. Girardi, R. Demarco, P. Rosati, and S. Borgani. *Astronomy and Astrophysics*, 442(1):29–41, 2005.

O. Y. Gnedin. *The Astrophysical Journal*, 582(1):141–161, Jan. 2003.

Gravity Collaboration, A. Amorim, M. Bauböck, W. Brandner, Y. Clénet, R. Davies, P. T. de Zeeuw, J. Dexter, A. Eckart, F. Eisenhauer, and N. M. e. a. Förster Schreiber. *Astronomy and Astrophysics*, 643:A154, Nov. 2020a.

Gravity Collaboration, O. Pfuhl, R. Davies, J. Dexter, H. Netzer, S. Hönig, D. Lutz, M. Schartmann, E. Sturm, A. Amorim, W. Brandner, Y. Clénet, P. T. de Zeeuw, A. Eckart, and F. e. a. Eisenhauer. *Astronomy and Astrophysics*, 634:A1, Feb. 2020b.

B. Groves, T. Heckman, and G. Kauffmann. *Monthly Notices of the Royal Astronomical Society*, 371:1559–1569, 2006.

J. E. Gunn and I. Gott, J. Richard. *The Astrophysical Journal*, 176:1, Aug. 1972.

C. M. Harrison, D. M. Alexander, J. R. Mullaney, J. P. Stott, A. M. Swinbank, V. Arumugam, F. E. Bauer, R. G. Bower, A. J. Bunker, and R. M. Sharples. *Monthly Notices of the Royal Astronomical Society*, 456(2):1195–1220, Feb. 2016.

C. M. Harrison, H. L. Johnson, A. M. Swinbank, J. P. Stott, R. G. Bower, I. Smail, A. L. Tiley, A. J. Bunker, M. Cirasuolo, D. Sobral, R. M. Sharples, P. Best, M. Bureau, M. J. Jarvis, and G. Magdis. *Monthly Notices of the Royal Astronomical Society*, 467(2):1965–1983, May 2017.

T. M. Heckman. *Astronomy and Astrophysics*, 500:187–199, July 1980.

B. P. Holden, G. D. Illingworth, M. Franx, J. P. Blakeslee, M. Postman, D. D. Kelson, A. van der Wel, R. Demarco, D. K. Magee, A. Tran, K. V. Zirm, H. Ford, P. Rosati, and N. Homeier. *The Astrophysical Journal*, 670(1):190–205, Nov. 2007.

P. F. Hopkins, L. Hernquist, T. J. Cox, T. Di Matteo, B. Robertson, and V. Springel. *The Astrophysical Journal Supplement Series*, 163(1):1–49, Mar. 2006.

P. F. Hopkins, L. Hernquist, T. J. Cox, and D. Kereš. *The Astrophysical Journal Supplement Series,*, 175(2):356–389, Apr. 2008.

R. C. W. Houghton. *Monthly Notices of the Royal Astronomical Society*, 451(4): 3427–3436, Aug. 2015.

M. J. Jee, R. L. White, N. Benítez, H. C. Ford, J. P. Blakeslee, P. Rosati,

R. Demarco, and G. D. Illingworth. *The Astrophysical Journal*, 618(1):46–67, Jan. 2005.

I. Jørgensen, M. Bergmann, R. Davies, J. Barr, M. Takamiya, and D. Crampton. *The Astrophysical Journal*, 129(3):1249–1286, Mar. 2005.

G. Kauffmann, T. M. Heckman, C. Tremonti, J. Brinchmann, S. Charlot, S. D. M. White, S. E. Ridgway, J. Brinkmann, M. Fukugita, P. B. Hall, Ivezić, G. T. Richards, and D. P. Schneider. *Monthly Notices of the Royal Astronomical Society*, 346(4):1055–1077, 2003.

K. Kawasaki, T. Nagao, Y. Toba, K. Terao, and K. Matsuoka. *The Astrophysical Journal*, 842:44, 2017.

L. J. Kewley, M. A. Dopita, R. S. Sutherland, C. A. Heisler, and J. Trevena. *The Astrophysical Journal*, 556(1):121–140, 2001a.

L. J. Kewley, B. Groves, G. Kauffmann, and T. Heckman. *Monthly Notices of the Royal Astronomical Society*, 372(3):961–976, 2006.

E. Y. Khachikian and D. W. Weedman. *The Astrophysical Journal*, 192:581–589, 1974.

J. Kormendy and L. C. Ho. *Annual Review Astronomy and Astrophysics*, 51(1): 511–653, Aug. 2013.

R. B. Larson, B. M. Tinsley, and C. N. Caldwell. *The Astrophysical Journal*, 237: 692–707, May 1980.

D. Lynden-Bell. *Nature*, 223(5207):690–694, 1969.

P. Madau and M. Dickinson. *Annual Review of Astronomy and Astrophysics*, 52 (1):415–486, 2014.

I. Marinova and S. Jogee. *The Astrophysical Journal*, 659:1176–1197, 2007.

P. Martini, E. D. Miller, M. Brodwin, S. A. Stanford, A. H. Gonzalez, M. Bautz, R. C. Hickox, D. Stern, P. R. Eisenhardt, A. Galametz, D. Norman, B. T. Jannuzi, A. Dey, S. Murray, C. Jones, and B. M. J. I. *The Astrophysical Journal*, 768(1):1, May 2013.

Matsuoka, K., Nagao, T., Maiolino, R., Marconi, A., and Taniguchi, Y. *Astronomy and Astrophysics*, 503(3):721–730, 2009.

B. J. Maughan, L. R. Jones, H. Ebeling, E. Perlman, P. Rosati, C. Frye, and C. R. Mullis. *The Astrophysical Journal*, 587(2):589–604, Apr. 2003.

S. Mei, S. A. Stanford, B. P. Holden, A. Raichoor, M. Postman, F. Nakata, A. Finoguenov, H. C. Ford, G. D. Illingworth, T. Kodama, P. Rosati, M. Tanaka, M. Huertas-Company, A. Rettura, F. Shankar, E. R. Carrasco, R. Demarco, P. Eisenhardt, M. J. Jee, Y. Koyama, and R. L. White. *The Astrophysical Journal*, 754(2):141, Aug. 2012.

A. Merloni, G. Rudnick, and T. Di Matteo. *Monthly Notices of the Royal Astronomical Society*, 354(3):L37–L42, Nov. 2004.

D. Merritt. *The Astrophysical Journal*, 264:24–48, Jan. 1983.

B. Moore, N. Katz, G. Lake, A. Dressler, and A. Oemler. *Nature*, 379(6566): 613–616, 1996.

Nagao, T., Maiolino, R., and Marconi, A. *Astronomy and Astrophysics*, 2006.

J. B. Nantais, H. Flores, R. Demarco, C. Lidman, P. Rosati, and M. J. Jee. *Astronomy and Astrophysics*, 555:A5, 2013.

B. Neichel, F. Hammer, M. Puech, H. Flores, M. Lehnert, A. Rawat, Y. Yang, R. Delgado, P. Amram, C. Balkowski, C. Cesarsky, H. Dannerbauer, I. Fuentes-Carrera, B. Guiderdoni, A. Kembhavi, Y. C. Liang, N. Nesvadba, G. Östlin, L. Pozzetti, C. D. Ravikumar, S. di Serego Alighieri, D. Vergani, J. Vernet, and H. Wozniak. *Astronomy and Astrophysics*, 484(1):159–172, 2008.

H. Netzer. *Annual Review of Astronomy and Astrophysics*, 53:365–408, Aug. 2015.

S. Oh, K. Oh, and S. K. Yi. *The Astrophysical Journal Supplement Series*, 198:4, 2011.

D. E. Osterbrock. *The Astrophysical Journal*, 249:462–470, 1981.

C. Y. Peng, L. C. Ho, C. D. Impey, and H.-W. Rix. *The Astrophysical Journal*, 124(1):266–293, 2002.

L. Pentericci, M. Castellano, N. Menci, S. Salimbeni, T. Dahlen, A. Galametz, P. Santini, A. Grazian, and A. Fontana. *Astronomy and Astrophysics*, 552:A111, Apr. 2013.

B. M. Peterson. *An Introduction to Active Galactic Nuclei*. Cambridge University Press, 1997.

B. M. Poggianti, A. Moretti, M. Gullieuszik, J. Fritz, Y. Jaffé, D. Bettoni, G. Fasano, C. Bellhouse, G. Hau, B. Vulcani, and et al. *The Astrophysical Journal*, 844(1):48, 2017.

M. Postman and M. J. Geller. *The Astrophysical Journal*, 281:95–99, June 1984.

M. Postman, M. Franx, N. J. G. Cross, B. Holden, H. C. Ford, G. D. Illingworth, T. Goto, R. Demarco, P. Rosati, J. P. Blakeslee, K.-V. Tran, and et al. *The Astrophysical Journal*, 623(2):721–741, apr 2005.

M. Radovich, B. Poggianti, Y. L. Jaffé, A. Moretti, D. Bettoni, M. Gullieuszik, B. Vulcani, and J. Fritz. *Monthly Notices of the Royal Astronomical Society*, 486(1):486–503, 03 2019.

D. O. Richstone. *The Astrophysical Journal*, 204:642–648, Mar. 1976.

R. A. Riffel, T. Storchi-Bergmann, and C. Winge. *Monthly Notices of the Royal Astronomical Society*, 430(3):2249–2261, 02 2013.

M. Rodrigues, F. Hammer, H. Flores, M. Puech, and E. Athanassoula. *Monthly Notices of the Royal Astronomical Society*, 465:1157–1180, 2016.

Rudolf, N., Günther, H. M., Schneider, P. C., and Schmitt, J. H. M. M. *Astronomy and Astrophysics*, 585:A113, 2016.

K. Sakamoto, S. K. Okumura, S. Ishizuki, and N. Z. Scoville. *The Astrophysical Journal*, 525:691–701, 1999.

K. Schawinski, M. Koss, S. Berney, and L. F. Sartori. *Monthly Notices of the Royal Astronomical Society*, 237:692–707, 2015.

C. K. Seyfert. *The Astrophysical Journal*, 97:28, jan 1943.

K. L. Shapiro, R. Genzel, N. M. Förster Schreiber, L. J. Tacconi, N. Bouché, G. Cresci, R. Davies, F. Eisenhauer, P. H. Johansson, D. Krajnović, D. Lutz, T. Naab, N. Arimoto, S. Arribas, A. Cimatti, L. Colina, E. Daddi, O. Daigle, D. Erb, O. Hernandez, X. Kong, M. Mignoli, M. Onodera, A. Renzini, A. Shapley, and C. Steidel. *The Astrophysical Journal*, 682(1):231–251, July 2008.

R. Sharples, R. Bender, A. Agudo Berbel, N. Bezawada, R. Castillo, M. Cirasuolo,

G. Davidson, R. Davies, M. Dubbeldam, A. Fairley, G. Finger, N. Förster Schreiber, and et al. *The Messenger*, 151:21–23, Mar. 2013.

R. M. Sharples, R. Bender, M. D. Lehnert, S. K. R. Howat, M. N. Bremer, R. L. Davies, R. Genzel, R. Hofmann, R. J. Ivison, R. Saglia, and N. A. Thatte. pages 1179 – 1186. International Society for Optics and Photonics, 2004.

Y.-K. Sheen, R. Smith, Y. Jaffé, M. Kim, S. K. Yi, P.-A. Duc, J. Nantais, G. Candlish, R. Demarco, and E. Treister. *Astrophysical Journal Letters*, 840 (1):L7, May 2017.

K. Sheth, M. W. Regan, N. Z. Scoville, and L. E. Strubbe. *Astrophysical Journal Letters*, 592:L13–L16, 2003.

G. A. Shields. *The Publications of the Astronomical Society of the Pacific*, 111 (760):661–678, June 1999.

I. Shlosman, J. Frank, and M. B. Begelman. *Nature*, 338:45–47, 1989.

R. S. Somerville and R. Davé. *Annual Review Astronomy and Astrophysics*, 53: 51–113, Aug. 2015.

J. P. Stott, A. M. Swinbank, H. L. Johnson, A. Tiley, G. Magdis, R. Bower, A. J. Bunker, M. Bureau, C. M. Harrison, M. J. Jarvis, R. Sharples, I. Smail, D. Sobral, P. Best, and M. Cirasuolo. *Monthly Notices of the Royal Astronomical Society*, 457(2):1888–1904, Apr. 2016.

J. P. Torres-Papaqui, R. Coziol, F. o. J. Romero-Cruz, A. C. Robleto-Orús, G. Escobar-Vásquez, A. Morales-Vargas, J. J. Trejo-Alonso, M. Chow-Martínez, and K. A. Cutiva-Alvarez. *The Astrophysical Journal*, 160(4):176, Oct. 2020.

E. Treister, P. Natarajan, D. B. Sanders, C. M. Urry, K. Schawinski, and J. Kartaltepe. *Science*, 328(5978):600, Apr. 2010.

E. Treister, K. Schawinski, C. M. Urry, and B. D. Simmons. *The Astrophysical Journal*, 758(2):L39, Oct 2012.

C. A. Tremonti, T. M. Heckman, G. Kauffmann, J. Brinchmann, S. Charlot, S. D. M. White, M. Seibert, E. W. Peng, D. J. Schlegel, A. Uomoto, M. Fukugita, and J. Brinkmann. *The Astrophysical Journal*, 613(2):898–913, Oct. 2004.

C. M. Urry and P. Padovani. *Publications of the Astronomical Society of the Pacific*, 107:803, Sept. 1995.

A. van der Wel, B. P. Holden, M. Franx, G. D. Illingworth, M. P. Postman, D. D. Kelson, I. Labbe, S. Wuyts, J. P. Blakeslee, and H. C. Ford. *The Astrophysical Journal*, 670(1):206–220, nov 2007.

L. van Zee, J. J. Salzer, and M. P. Haynes. *Astrophysical Journal Letters*, 497(1): L1–L4, Apr. 1998.

E. Wisnioski, N. M. Förster Schreiber, S. Wuyts, E. Wuyts, K. Bandara, D. Wilman, R. Genzel, R. Bender, R. Davies, M. Fossati, P. Lang, J. T. Mendel, A. Beifiori, G. Brammer, J. Chan, M. Fabricius, Y. Fudamoto, S. Kulkarni, J. Kurk, D. Lutz, E. J. Nelson, I. Momcheva, D. Rosario, R. Saglia, S. Seitz, L. J. Tacconi, and P. G. van Dokkum. *The Astrophysical Journal*, 799(2):209, Feb. 2015.

E. Wisnioski, N. M. Förster Schreiber, M. Fossati, J. T. Mendel, D. Wilman, R. Genzel, R. Bender, S. Wuyts, R. L. Davies, H. Übler, K. Bandara, A. Beifiori, S. Belli, G. Brammer, J. Chan, R. I. Davies, M. Fabricius, A. Galametz, P. Lang, D. Lutz, E. J. Nelson, I. Momcheva, S. Price, D. Rosario, R. Saglia, S. Seitz, T. Shimizu, L. J. Tacconi, K. Tadaki, P. G. van Dokkum, and E. Wuyts. *The Astrophysical Journal*, 886(2):124, Dec. 2019.

X.-G. Zhang, D. Deborah, W. Ting-Gui, and K. Guinevere. *Monthly Notices of the Royal Astronomical Society*, 397:1510–1520, 2009.